Chemical Engineering Science 338 (2027) 124805

Contents lists available at ScienceDirect

Chemical Engineering Science

journal homepage: www.elsevier.com/locate/ces

Assessment of class- and method-of-moments-based population balance models for enhancing predictive accuracy in pseudo-2D polydisperse bubbly flow systems☆

Lydia Becka[a,b,*], Yannik Danner[a], Ralf Peters[a,b], Thomas E. Müller[c]

[a] Forschungszentrum Jülich GmbH, Electrochemical Process Engineering (IET-4), Wilhelm-Johnen-Straße, 52425 Jülich, Germany
[b] Ruhr-Universität Bochum, Synthetische Kraftstoffe, Universitätsstraße 150, 44801 Bochum, Germany
[c] Ruhr-Universität Bochum, Carbon Sources and Conversion, Universitätsstraße 150, 44801 Bochum, Germany

ARTICLE INFO

Keywords:
Gas-liquid bubble columns
Euler-Euler approach
Computational fluid dynamics
Population balance modeling
Bubble size distribution
Polydispersity in multiphase flow

ABSTRACT

Even though multiphase reactors are essential for gas–liquid processes in the chemical and energy industries, their hydrodynamics remain difficult to model. Accurate prediction of polydisperse bubbly flows requires coupling Euler-Euler computational fluid dynamics (CFD) with population balance models (PBMs). Pseudo-two-dimensional bubble columns provide a geometrically confined, experimentally accessible benchmark for assessing such models. This work establishes a methodological benchmark, providing a comparison of class-based and moment-based PBM formulations within a pseudo-2D Euler-Euler CFD framework, including assessment of structural model behavior, sensitivity to kernel formulations, and computational cost.

The single-population class method with the Laakkonen breakage kernel and the Prince and Blanch coalescence kernel provides the most accurate volume-averaged predictions, with an absolute deviation below 0.6 vol % for gas holdup and a relative deviation below 8 % for the Sauter mean diameter. Extending the class method to three bubble populations resolves size-dependent slip velocities but does not improve volume-averaged predictions. By contrast, the single-population Method-of-Moments overpredicts bubble sizes. In the multifluid DQMoM formulation, the dispersed populations become increasingly similar during the simulation, resulting in substantially weaker size-dependent segregation than in the corresponding class-based multifluid approach. Inclusion of lateral lift degrades accuracy across all models.

Overall, pseudo-2D bubble columns are established as stringent benchmark systems for CFD-PBM coupling, enabling a structural assessment of PBM formulations under confinement. The results show that predictive capability depends on both PBM formulation and hydrodynamic population resolution. Class-based approaches are preferable for capturing segregation, whereas moment-based formulations offer greater computational efficiency for predicting global reactor behavior.

1. Introduction

The global transition toward harnessing sustainable energy and resources has driven the urgency to optimize industrial processes and minimize their environmental impact (Markewitz et al., 2012; Robinius et al., 2017; Tomkins and Müller, 2019). Gas-liquid contactors are widely employed in industrial operations where interfacial mass transfer between a dispersed gas phase and a continuous liquid phase governs overall performance. Typical examples include amine-based CO_2 absorption, physical gas absorption and stripping processes, air-sparged bioreactors, and bubble-column contactors used in environmental and wastewater treatment, where gas–liquid mass transfer is rate-controlling (McClure et al., 2013; Shah et al., 1982; Besagni et al., 2018).

In these systems, gas is commonly introduced at the reactor bottom, forming a polydisperse bubbly flow whose hydrodynamics – governed by bubble size, bubble-size distribution, and spatial gas distribution – directly determine gas holdup, interfacial area, mass transfer efficiency, energy consumption, and pressure drop (L. Gemello, Modelling of the Hydrodynamics of Bubble Columns Using a Two-Fluid Model Coupled with a Population Balance Approach, PhD thesis, Université Claude Bernard Lyon 1, Lyon, France and Politecnico di Torino, Turin, Italy,

☆ This article is part of a special issue entitled: 'PBM 2025 ? Ramki Tribute' published in Chemical Engineering Science.

* Corresponding author.
E-mail address: l.becka@fz-juelich.de (L. Becka).

https://doi.org/10.1016/j.ces.2026.124805
Received 31 March 2026; Received in revised form 23 June 2026; Accepted 30 June 2026
Available online 29 July 2026
0009-2509/© 2026 The Author(s). Published by Elsevier Ltd. This is an open access article under the CC BY license (http://creativecommons.org/licenses/by/4.0/).

Nomenclature

Abbreviations

2D	Two −Dimensional
BSD	Bubble Size Distribution
C1, C3	Class method models with one or three bubble populations
CFD	Computational Fluid Dynamics
DQMoM	Direct Quadrature Method-of-Moments
LDA	Laser Doppler Anemometry
LL	Model variant including lateral lift force
M1, M3	Method-of-Moments models with one or three bubble populations
MEA	Mean Absolute Error
PBM	Population Balance Model
PC-SIMPLE	Phase Coupled Semi-Implicit Method for Pressure-Linked Equations
PRESTO!	Pressure Staggering Option
QMoM	Quadrature Method-of-Moments
QUICK	Quadratic Upwind Interpolation for Convective Kinematics
URANS	Unsteady Reynolds-Averaged Navier-Stokes
RNG	Renormalization Group
RMSE	Root Mean Square Error
UDF	User-Defined Function

Symbols

B	*Birth term*
C_D	*Effective drag force coefficient*
$C_{D,0}$	*Drag force coefficient for an isolated bubble*
C_{LL}	*Lateral lift force coefficient*
C_{TD}	*Turbulent dispersion force coefficient*
C_{VM}	*Virtual mass force coefficient*
D	*Death term*
$\frac{D_q}{Dt}$	*Material derivative following the motion of phase q*
E_o	*Eötvös number*
$\boldsymbol{F}_q$	*Interfacial momentum source term for phase q*
$\boldsymbol{F}_D$	*Drag force*
$\boldsymbol{F}_{LL}$	*Lateral lift force*
$\boldsymbol{F}_{TD}$	*Turbulent dispersion force*
$\boldsymbol{F}_{VM}$	*Virtual mass force*
M_j	*Moment of j-th order of the bubble size distribution*
N	*Number of quadrature points*
$N_i(\boldsymbol{x},t)$	*Class-wise number density*
$\boldsymbol{R}$	*Internal coordinates representing intrinsic bubble properties (e.g., characteristic length, volume)*
Re	*Reynolds number*
$S(d,\boldsymbol{x},t)$	*Source term in PBM*
S_{12}	*Collision cross-section*
V	*Volume*
$\boldsymbol{X}$	*External coordinates describing the spatial position of bubbles*
b	*Breakage*
c	*Coalescence*
d	*Bubble diameter*
$\overline{d}$	*Arithmetic mean bubble diameter*
d_{32}	*Sauter mean diameter*
d_{eq}	*Equivalent bubble diameter*
$\boldsymbol{g}$	*Gravitational acceleration vector*
g_1, g_2, g_3	*Individual gas phases representing different bubble size populations*
$g(d)$	*Breakage frequency*
$h(d,d')$	*Coalescence rate*
h_0	*Collision rate*
h_{crit}	*Critical rupture thickness of the liquid film*
h_f	*Initial liquid film thickness*
i	*Individual bubble size classes*
j	*Order of moment*
k	*Turbulent kinetic energy*
l	*Liquid phase*
$n(d,\boldsymbol{x},t)$	*Number-based density function in PBM*
p	*Pressure*
q	*Phase index*
t	*Time*
t_D	*Film drainage time*
$\boldsymbol{u_q}$	*Velocity of phase q*
u_{rel}	*Relative velocity between phases*
$u_{s,g}$	*Superficial gas velocity*
w_i	*Weight fractions*
α_q	*Volume fraction of phase q*
$\beta(d\|d')$	*Daughter size distribution*
ε	*Turbulent kinetic energy dissipation rate*
λ	*Coalescence efficiency*
μ_q	*Dynamic viscosity of phase q*
$\mu_{l,turb}$	*Turbulent viscosity of liquid phase*
ν_q	*Kinematic viscosity of phase q*
ρ_q	*Density of phase q*
σ	*Surface tension*
σ_{TD}	*Turbulent dispersion Schmidt number (model constant)*
τ	*Contact time*
τ_q	*Stress tensor of phase q*

2018; McClure et al., 2013; Weiske, 2022; Wang and Wang, 2017). Accurately predicting these hydrodynamics remains challenging because of the complex interplay between bubble coalescence, breakup, turbulence, and size-dependent interfacial forces (Weiske, 2022; Shah et al., 1982).

Increasing superficial gas velocity, turbulence intensity and bubble–bubble interactions enhance breakup and coalescence dynamics and, consequently lead to broader bubble size distributions (BSD) and pronounced size-dependent bubble migration (Besagni et al., 2018; Liao and Lucas, 2009; Liao and Lucas, 2010). Moreover, non-drag forces such as lateral lift, turbulent dispersion, and wall lubrication also play a decisive role in governing these size-dependent bubble dynamics and spatial gas distributions (Ziegenhein et al., 2018; Lucas et al., 2020; Hessenkemper et al., 2021; Rzehak et al., 2015). Since the resulting size dependence introduces nonlinear momentum coupling between the dispersed and continuous phases, robust representation of bubble-size effects is essential for reliable reactor analysis and design.

Computational fluid dynamics (CFD) based on the Euler-Euler unsteady Reynolds-averaged Navier-Stokes (URANS) framework is widely used to model such flows. Gas-phase polydispersity is typically incorporated through population balance modeling (PBM). There are two major PBM families: the class method, which resolves bubble sizes as discrete classes, and the Method-of-Moments, which describes statistical moments of the BSD without resolving individual sizes (Ramkrishna, 2000). Both approaches have been applied extensively in bubble-column simulations (Pfleger and Becker, 2001; Sanyal et al., 2005; Marchisio and Fox, 2013; Besagni et al., 2018), yet predicted holdups, BSDs, and flow structures vary significantly across studies. While Method-of-Moments-based approaches are attractive because of their computational efficiency, class-based formulations provide explicit access to size-conditioned hydrodynamics. However, their relative structural suitability, particularly in flow regimes with strong size-dependent hydrodynamics, remains insufficiently understood.

Despite extensive application of CFD-PBM approaches to bubble columns, it remains unclear how much population resolution is actually required to accurately capture size-dependent hydrodynamics. Existing studies typically investigate either class-based PBMs (including MUSIG-type implementations) or Method-of-Moments formulations individually, making it difficult to distinguish between effects originating from the representation of the bubble size distribution and those arising from the hydrodynamic resolution of bubble populations.

In particular, single-population PBMs account for bubble-size evolution but enforce a common gas velocity field for all bubble sizes, whereas population-resolved multifluid approaches provide separate momentum balances for different bubble populations but are often applied without dynamic population balance modeling. Consequently, the interaction between bubble-size representation, hydrodynamic population resolution, and computational effort has not yet been systematically assessed for confined bubbly flows.

The objective of the present work is therefore to establish a systematic methodological benchmark for assessing the influence of hydrodynamic population resolution on CFD-PBM predictions of confined bubbly flows. Class-based and Method-of-Moments formulations are compared within a consistent pseudo-2D Euler-Euler framework, ranging from single-population approaches employing a shared gas momentum equation to population-resolved multifluid formulations with separate gas phases representing different bubble-size groups.

This setup enables the individual and combined effects of bubble-size representation, hydrodynamic population resolution, interfacial-force modeling, and computational cost to be evaluated under identical operating conditions. Model predictions are validated against experimental data and analyzed with respect to both global quantities and local segregation phenomena. Particular emphasis is placed on identifying the minimum level of hydrodynamic population resolution required to reproduce size-dependent bubble dynamics under geometrical confinement.

By isolating the effects of PBM structure, multifluid coupling, and confinement, this study provides clear, geometry-specific guidance on the suitability and limitations of common PBM formulations and establishes pseudo-2D bubble columns as effective diagnostic benchmarks for CFD-PBM coupling in multiphase reactor modeling.

2. Modeling Approach

2.1. State of the Art and Open Modeling Challenges

Despite the large body of CFD-PBM research, several aspects of polydisperse bubbly-flow modeling remain insufficiently resolved. Existing comparisons of the class method and the Method-of-Moments have been conducted primarily for three-dimensional bubble columns, where bubble-size distributions are relatively symmetric and size segregation is moderate (Pfleger and Becker, 2001; Sanyal et al., 2005). These studies typically employ single-population PBMs, in which all bubble sizes share a common momentum equation (Pfleger and Becker, 2001; Marchisio and Fox, 2013). Such formulations are inherently limited in their ability to reproduce divergent bubble trajectories arising from size-dependent interfacial forces, including the well-documented reversal of the lift force at a characteristic bubble diameter (Ziegenhein et al., 2018; Ziegenhein and Lucas, 2019; Lucas et al., 2020; Hessenkemper et al., 2021).

Under geometric confinement, such as in pseudo-2D bubble columns, these mechanisms become strongly amplified. Reduced column depth increases pitch of near-wall shear and pressure gradients, enhances lateral lift and wall-lubrication effects, and leads to pronounced size segregation and core-annular flow structures (Ziegenhein et al., 2018; Liu et al., 2019). These conditions challenge PBM closures that implicitly assume weak segregation and motivate the use of multifluid, population-resolved PBM formulations, in which selected bubble populations (defined by size ranges) evolve with distinct momentum balances (Krepper et al., 2008; Lucas et al., 2011; Lucas et al., 2020).

While population-resolved multifluid approaches resolve size-dependent hydrodynamics using multiple Eulerian fields representing distinct bubble populations with fixed representative diameters, they typically neglect bubble-size evolution. Conversely, population balance models resolve bubble-size distributions but are most often coupled with single-population formulations enforcing a common velocity field. Consequently, the influence of bubble-size representation and hydrodynamic population resolution cannot easily be separated, and both aspects are rarely addressed simultaneously within a fully coupled framework (Sanyal et al., 2005; Buffo et al., 2013; Marchisio and Fox, 2013).

Pseudo-2D bubble columns, however, are particularly well suited for such investigations, because geometric confinement amplifies size-dependent hydrodynamic effects while remaining experimentally accessible. A range of experimental studies has demonstrated pronounced lateral structuring and bubble-size segregation under confined conditions, using techniques such as LDA measurements (Becker et al., 1999), high-speed imaging (Buwa and Ranade, 2002), pressure-based regime mapping (Díaz et al., 2008), and particle-tracking- and visualization-based flow reconstruction (Cachaza et al., 2008; Upadhyay et al., 2013).

These datasets provide geometry-consistent and well-resolved reference cases in which confinement-induced effects are experimentally quantified, making pseudo-2D systems particularly suitable for systematically assessing the capability of different PBM formulations to reproduce size-dependent hydrodynamics.

Recent modeling perspectives advocate modular, component-resolved validation strategies, in which hydrodynamics, interfacial forces, and population-balance closures are assessed independently before being integrated into a full CFD-PBM framework (Mappas et al., 2025).

2.2. Modeling Scope and Strategy

To assess the performance of hydrodynamic models, this work adopts a systematic modeling framework to evaluate population balance modeling strategies for polydisperse bubbly flows under well-defined pseudo-2D hydrodynamic conditions. Using transient Euler-Euler URANS simulations performed in ANSYS Fluent, this study implements and compares class-based and Method-of-Moments-based PBM formulations. Specifically, the modeling framework considers:

- Class method vs. Method-of-Moments,
- Single-population vs. population-resolved multifluid PBM configurations,
- Influence of lateral lift under confinement, and
- Computational cost vs. predictive accuracy
- Hydrodynamic population resolution vs. bubble-size representation.

A digital twin of the pseudo-2D experiments of Díaz (Díaz et al., 2008) and Cachaza (Cachaza et al., 2008) is constructed to enable controlled, geometry-consistent comparison, eliminating confounding variations in sparger design or column depth that would otherwise obscure PBM-related differences. Qualitative comparison with independent pseudo-2D studies is first employed to assess the physical plausibility of predicted segregation patterns and flow structures, followed by quantitative evaluation using measured gas holdup and Sauter mean diameter.

By isolating hydrodynamic and population-balance effects under confined conditions, the applied modeling approach enables systematic identification of structural differences between PBM formulations and supports evidence-based guidance for their use in CFD-PBM simulations of gas-liquid reactors.

2.3. Numerical Framework and Solver Setup

Physical and numerical simulations were performed using Ansys Fluent 2023 R2 on a high-performance workstation (Intel Xeon Gold 6154, 72 cores, 3.0 GHz, Windows 10 Pro). Custom user-defined functions (UDFs) were implemented *via* the integrated C++ interface to extend the solver capabilities.

2.3.1. Geometry and Boundary Conditions

The pseudo-2D gas-liquid bubble column was designed based on the experimental configurations of Díaz et al. (Díaz et al., 2008) and Cachaza et al. (Cachaza et al., 2008). The shallow column depth enforces a pseudo-2D flow field, which amplifies confinement-induced, size-dependent hydrodynamic effects while remaining experimentally well characterized. This makes the geometry particularly well suited as a benchmark configuration for assessing population-balance formulations under controlled conditions.

Since the overall gas holdup remains below 4.1 vol % under the investigated conditions, as confirmed by the reference experiments (Díaz et al., 2008) and the present simulations (see Section 3.1), changes in liquid level and gas dissolution are negligible. Consequently, the column height was truncated to the initial liquid level, and the free surface was not explicitly resolved to reduce computational cost and improve numerical stability.

The geometry (Fig. 1) measured 0.20 m (width), 0.45 m (height), and 0.04 m (depth), corresponding to an effective liquid volume of 3.6×10^{-3} m^3. Demineralized water was considered as the continuous phase and air as the dispersed phase. Gas density was assumed constant, since the hydrostatic pressure variation over the column height of 0.45 m results in only minor density changes, which are negligible compared to other modeling uncertainties. Surface tension was set to 0.072 N m^{-1} (Lide, 2009). Gravity was included to represent buoyancy-driven flow.

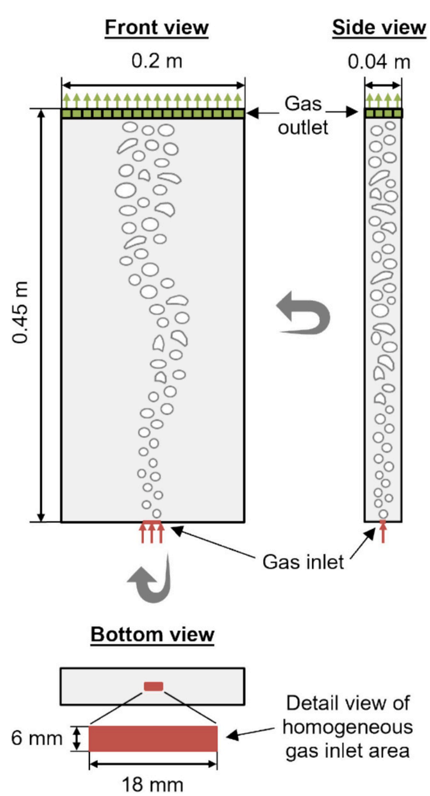

Fig. 1. Geometry of the pseudo-2D bubble column with front, side, and bottom views. The schematic illustrates the column dimensions, the homogeneous gas inlet area at the column bottom, and the degassing outlet at the column top; bubble shapes are illustrative and not to scale.

Gas was introduced uniformly through a rectangular inlet (18 mm × 6 mm) at the column bottom.

The inlet area was selected to represent the total gas injection area of the experimental sparger while providing a numerically stable boundary condition for the Euler-Euler simulations. Explicit resolution of the individual sparger holes would introduce highly localized gas injection and steep phase-fraction gradients, which are known to cause numerical instabilities in Euler-Euler models (Hlawitschka et al., 2016; Buffo et al., 2016). Since the objective of the present study is the assessment of PBM formulations rather than the detailed modeling of bubble formation at the sparger, an equivalent inlet representation with uniform gas distribution was considered appropriate.

To ensure stable initialization, a gas holdup of 0.5 was imposed in the inlet cells, reflecting the volume-averaged phase representation inherent to Euler-Euler models, in which sharp phase interfaces are not explicitly resolved (Buffo et al., 2013; Cachaza et al., 2009).

Superficial gas velocities, defined based on the empty column cross-sectional area, of 2.4, 11.9, and 21.3 mm s^{-1} were investigated. Corresponding initial arithmetic mean bubble diameters $\overline{d}$ were estimated using the correlation of Geary and Rice (Geary and Rice, 1991). The experimental sparger consists of eight holes with a diameter of 1 mm; this diameter was therefore used to estimate the initial bubble size. For orifice diameters in this range, bubble formation is governed by a force balance and becomes only weakly dependent on the exact orifice size (Wilkinson et al., 1992). The resulting mean bubble diameters were 6.3, 8.3, and 10.0 mm.

For initialization of the population balance model, these mean diameters were used to define a log-normal inlet BSD with a standard deviation of 0.15 $\overline{d}$, in line with typical inlet dispersions reported for comparable configurations (Petitti et al., 2010). This distribution ensured consistent initial conditions across all simulations; the subsequent evolution of the BSD and the associated bubble populations was governed by the population balance model through coalescence and breakup.

At the outlet, a degassing boundary condition was applied, whereby gas volume fractions reaching the top cell layer were removed from the computational domain, while the liquid phase remained confined within the column.

2.3.2. Numerical Simulation Procedure

The simulations were conducted in a transient framework with up to fifty iterations per time step. Phase coupling was achieved using the Phase-Coupled Semi-Implicit Method for Pressure-Linked Equations (PC-SIMPLE). Temporal discretization employed a first-order implicit scheme. This choice was made deliberately to reduce computational cost and ensure a fair comparison of different modeling strategies. While higher-order schemes can improve accuracy, they are rarely applied in large-scale multiphase simulations due to their significantly higher computational demand. Spatial discretization followed established practice in Euler-Euler multiphase CFD: Gradients were computed with the Green-Gauss node-based method; Pressure and volume fraction were interpolated with PRESTO! and QUICK schemes, respectively. In addition, turbulence quantities were resolved with a first-order upwind scheme. Default under-relaxation factors recommended by ANSYS Fluent were applied to ensure numerical stability (ANSYS Inc., ANSYS Fluent User's Guide, Release, 2022). The full set of solver parameters is summarized in Table S1 in the Supplementary Information.

Each case was initialized for 20 s at the lowest superficial gas velocity using a monodisperse BSD with drag as the sole interfacial interaction to establish a numerically stable flow field. The full population balance model and the target gas velocity were then activated, followed by a further run-up period of 20 s to allow representative flow structures to develop. Time-averaging was subsequently performed over a 60 s interval, corresponding to simulated times between 40 and 100 s. This averaging window was selected because the initial transient behavior had fully decayed by this time and the monitored global quantities exhibited only small fluctuations around statistically stationary mean values thereafter. Consequently, the reported results are based exclusively on the quasi-stationary flow regime and are not affected by the initialization phase. The averaging procedure was applied solely during post-processing of the transient simulation results; the governing equations themselves were solved in fully transient form throughout the entire simulation.

The described numerical setup was applied to eight modeling configurations, varying in (i) bubble-size modeling approach (class method vs. Method-of-Moments), (ii) population resolution (single-population vs. population-resolved multifluid representation), and (iii) inclusion of the lateral lift force. A detailed overview of these model variants is provided in Section 3.

2.4. Hydrodynamic Modeling Framework

The hydrodynamics and bubble interactions in the pseudo-2D bubble column were modeled using a transient Euler-Euler multiphase framework coupled with an unsteady Reynolds-averaged Navier-Stokes (URANS) turbulence closure. The framework comprised conservation equations for mass and momentum, turbulence modeling, interfacial force formulations, and bubble size dynamics represented by a PBM.

2.4.1. Governing Equations

In the applied Euler-Euler multiphase model, the continuous liquid phase (l) and one or more Eulerian gas fields ($g_1, g_2, ..., g_q$) are treated as interpenetrating continua. In population-resolved formulations, these Eulerian gas fields represent distinct bubble populations defined by specified bubble-size ranges, each characterized by its own volume fraction and velocity field. This approach enables the explicit resolution of size-conditioned hydrodynamics and non-uniform gas flow behavior.

Throughout this work, Eulerian gas fields, thus, are interpreted as bubble populations rather than distinct physical gas phases. The terms single-population and population-resolved formulations are used to distinguish between models employing a single shared gas momentum equation for all bubble sizes and those resolving multiple gas momentum equations for different bubble populations. All formulations describe the same physical gas phase and differ only in the degree of hydrodynamic resolution applied to the bubble-size distribution.

For each phase $q \in \{l, g_1, g_2, ..., g_q\}$, the Reynolds-averaged continuity (Eq. (1) and momentum equations (Eq. (2) are solved within the transient Euler-Euler URANS framework and are expressed as (Date, 2005):

$$\frac{\partial}{\partial t}(\alpha_q \rho_q) + \nabla \bullet (\alpha_q \rho_q \boldsymbol{u}_q) = 0 \tag{1}$$

$$\frac{\partial}{\partial t}(\alpha_q \rho_q \boldsymbol{u}_q) + \nabla \bullet (\alpha_q \rho_q \boldsymbol{u}_q \otimes \boldsymbol{u}_q) = -\alpha_q \nabla p + \nabla \bullet \boldsymbol{\tau}_q + \alpha_q \rho_q \boldsymbol{g} + \boldsymbol{F}_q \tag{2}$$

Here, α_q, ρ_q and $\boldsymbol{u}_q$ denote the volume fraction, density, and velocity of phase q, respectively. The stress tensor $\boldsymbol{\tau}_q$ includes molecular and turbulent contributions. The interfacial momentum exchange term $\boldsymbol{F}_q$ accounts for drag and non-drag forces (see Section 2.4.3). Pressure p is assumed to be shared among all phases, and $\boldsymbol{g}$ denotes the gravitational acceleration vector.

2.4.2. Turbulence Modeling

Within the Euler-Euler URANS framework applied in this study, turbulence in the continuous liquid phase is modeled using the RNG k-ε turbulence model. This two-equation eddy-viscosity formulation solves transport equations for the turbulent kinetic energy k and its dissipation rate ε. Compared to the standard k-ε model, the RNG variant introduces an additional term in the ε-equation derived from renormalization group theory, improving performance in flows characterized by high strain rates, streamline curvature, and recirculation. These features are characteristic of bubble column reactors and pseudo-2D bubbly flows.

The suitability of the RNG k-ε model for heterogeneous gas-liquid systems has been demonstrated in numerous CFD and CFD-PBM studies, reporting robust numerical behavior and improved prediction of large-scale circulation structures and plume dynamics relative to the standard k-ε formulation (Yakhot and Orszag, 1986; Liu and Hinrichsen, 2014).

Turbulence transport equations are solved exclusively for the continuous liquid phase, consistent with the Euler–Euler URANS framework employed in this study. The resulting turbulent viscosity enters the multiphase momentum equations *via* phase-coupled source terms, thereby accounting for the influence of liquid-phase turbulence on bubble motion and interfacial momentum exchange.

Since the turbulence dissipation rate directly enters the breakup and coalescence kernels employed in the population balance model, the turbulence closure constitutes an integral part of the overall CFD-PBM framework (Buffo et al., 2013). The RNG k-ε model, together with the selected interfacial-force, breakup, and coalescence closures, represents a commonly applied baseline modeling approach for Euler-Euler simulations of bubbly flows (Rzehak et al., 2015; Yakhot and Orszag, 1986; Liu and Hinrichsen, 2014). While alternative turbulence closures may influence the resolved transient flow structures, local dissipation rates, and consequently the predicted bubble-size evolution, their assessment requires a corresponding re-evaluation of the overall closure-model combination and numerical resolution to ensure consistency between the resolved flow structures and the underlying model assumptions.

2.4.3. Interfacial Force Modeling

Interfacial forces govern momentum exchange between phases in Euler-Euler simulations and must be selected in accordance with the hydrodynamic regime and geometric constraints of the system. In population-resolved multifluid simulations, the interfacial-force closures are applied per bubble population, using the corresponding gas-field volume fraction and velocity.

In pseudo-2D bubble columns, reduced depth and wall proximity can alter bubble trajectories and modify the relative importance of individual force terms. The correlations applied in this study follow widely used formulations originally developed for unconfined three-dimensional flows. Although these models are commonly employed in confined systems and generally provide sufficient accuracy, their applicability under pseudo-2D conditions requires careful evaluation and is explicitly examined here.

In the following, interfacial force terms are consistently expressed as acting on the gas phase, with the corresponding liquid-phase contributions implied by sign reversal.

2.4.3.1. Drag Force. The dominant contribution in this system is the drag force $\boldsymbol{F}_D$ (Eq. (3) (Michaelides et al., 2022), which represents the resistance exerted by the continuous liquid phase against the relative motion of gas bubbles:

$$\boldsymbol{F}_D = \frac{3}{4}\frac{C_D \rho_l \alpha_g \alpha_l}{d}\left|\boldsymbol{u}_g - \boldsymbol{u}_l\right|(\boldsymbol{u}_g - \boldsymbol{u}_l) \tag{3}$$

The drag coefficient for an isolated bubble $C_{D,0}$ is modeled according to Tomiyama (Tomiyama, 1998), which provides reliable predictions for both spherical and deformed bubbles and is widely used in gas-liquid systems (L. Gemello, Modelling of the Hydrodynamics of Bubble Columns Using a Two-Fluid Model Coupled with a Population Balance Approach, PhD thesis, Université Claude Bernard Lyon 1, Lyon, France and Politecnico di Torino, Turin, Italy, 2018; Sanyal et al., 2005; Liu and Hinrichsen, 2014; Rzehak et al., 2017). This correlation accounts for the Eötvös number E_o (Eq. (4) and the bubble Reynolds number Re_B (Eq. (5); both of which are functions of the bubble diameter d:

$$E_o = \frac{\Delta \rho g d^2}{\sigma} \tag{4}$$

$$Re_B = \frac{\rho_l |\boldsymbol{u}_g - \boldsymbol{u}_l| d}{\mu_l} \tag{5}$$

Here, $\Delta\rho$ is the density difference between the liquid and gas phases, g is the magnitude of the gravitational acceleration, σ denotes the surface tension of the liquid phase, and μ_l the dynamic viscosity of the liquid.

The drag coefficient $C_{D,0}$ is then calculated as follows (Eq. (6) (Tomiyama, 1998).

$$C_{D,0} = \max\left[\min\left[\frac{24}{Re_B}\left(1 + 0.15Re_B^{0.687}\right), \frac{72}{Re_B}\right], \frac{8}{3}\frac{E_0}{E_0 + 4}\right] \tag{6}$$

For the investigated operating conditions, the overall gas holdup remains substantially below the threshold at which swarm effects become relevant. Although locally increased gas volume fractions may occur within the plume region, the volume-averaged holdup of the pseudo-2D column stays well below the approximately 20 vol % void fraction reported for the onset of swarm-dependent drag corrections (Roghair et al., 2013; Zhang et al., 2020). Accordingly, swarm effects are neglected and the isolated drag coefficient $C_{D,0}$ is used as the effective drag coefficient C_D.

In contrast to drag, which is comparatively well established in Euler-Euler simulations, non-drag forces exhibit pronounced size dependence and inconsistent effects on bubble migration (Borchers and Eigenberger, 2004; Tomiyama et al., 2002). Their influence is therefore examined in detail in the following sections.

2.4.3.2. Non-Drag Forces. Beyond drag, several additional interfacial forces contribute to bubble dynamics in Euler-Euler simulations. These include virtual mass, turbulent dispersion, and lateral lift, each representing different physical mechanisms of phase interaction. The corresponding models and their relevance for the present pseudo-2D configuration are outlined in the following.

The virtual mass force $\boldsymbol{F}_{VM}$ (Eq. 7) (Michaelides et al., 2022) accounts for the additional inertia of the surrounding liquid that is accelerated as a bubble changes velocity. A coefficient of $C_{VM} = 0.5$ is applied in accordance with common recommendations (Khan, 2014; Cheng et al., 2020).

$$\boldsymbol{F}_{VM} = C_{VM}\rho_l\alpha_g\alpha_l\left(\frac{D_g\boldsymbol{u}_g}{Dt} - \frac{D_l\boldsymbol{u}_l}{Dt}\right) \tag{7}$$

The operators $\frac{D_q}{Dt}$ denote material derivatives following the motion of phase q, combining local and convective acceleration. Although its influence on macroscopic flow structures is generally small, virtual mass improves the representation of relative phase acceleration and is known to enhance transient stability in Euler-Euler URANS simulations (Zhang et al., 2020). Recent assessments confirm its relevance in pseudo-2D systems, where confinement can amplify lateral accelerations (Liu et al., 2019; Lucas and Ziegenhein, 2019; Lucas et al., 2020).

The turbulent dispersion force $\boldsymbol{F}_{TD}$ (Eq. (8) (Michaelides et al., 2022) represents bubble spreading caused by turbulent liquid fluctuations and is modeled following Burns et al. (Burns et al., 2004), whose formulation has shown strong performance in pseudo-2D column simulations (Liu and Hinrichsen, 2014; Fletcher et al., 2017; Xu et al., 2013):

$$\boldsymbol{F}_{TD} = \frac{3}{4}C_{TD}\alpha_g\alpha_l\frac{C_D}{d}|\boldsymbol{u}_g - \boldsymbol{u}_l|\frac{\mu_{l,turb}}{\sigma_{TD}}\left(\frac{\nabla\alpha_g}{\alpha_g} - \frac{\nabla\alpha_l}{\alpha_l}\right) \tag{8}$$

Here $C_{TD} = 1$ and $\sigma_{TD} = 0.9$ are used, with the turbulent viscosity $\mu_{l,turb}$ taken from the RNG k-ε model. In shallow geometries, turbulent dispersion partially compensates for reduced lateral mixing and has been reported to gain importance under confinement (Liu et al., 2019; Buwa and Ranade, 2002).

Particular attention is given to the lateral lift force $\boldsymbol{F}_{LL}$ (Eq. (9) (Michaelides et al., 2022), which arises from velocity gradients in the surrounding liquid phase and acts perpendicular to the bubble slip velocity.

$$\boldsymbol{F}_{LL} = C_{LL}\rho_l\alpha_g\alpha_l(\boldsymbol{u}_g - \boldsymbol{u}_l) \times (\nabla \times \boldsymbol{u}_l) \tag{9}$$

In the present work, the lift force is modeled using the correlation by Tomiyama et al. (Tomiyama et al., 2002), which describes a size-dependent change in lift direction through the sign of the lift coefficient C_{LL}. The lift coefficient C_{LL} (Eq. (10) is defined piecewise as a function of the modified Eötvös number E_o', with the bubble Reynolds number Re_b(Eq. (5) (Tomiyama et al., 2002):

$$C_{LL} = \begin{cases} min\left[0.288tanh(0.121Re_B), f(E_o')\right] & for\ E_o' \leq 4 \\ f(E_o') & for\ 4 < E_o' \leq 10 \\ -0.27 & for\ 10 < E_o' \end{cases} \tag{10}$$

where the auxiliary function $f(E_o')$ is given by (Eq. (11):

$$f(E_o') = 0.00105E_o'^3 - 0.0150E_o'^2 - 0.0204E_o' + 0.474 \tag{11}$$

The modified Eötvös number E_o' is defined analogously to the classical Eötvös number (Eq. (4) but related to the longest axis of a deformed bubble d' (Eq. (12):

$$d' = d\sqrt{1 + 0.163E_o^{0.757}} \tag{12}$$

For air-water systems, the Tomiyama correlation (Tomiyama et al., 2002) predicts a sign change of the lift coefficient C_{LL} at a critical bubble diameter of approximately 5.8 mm. Consequently, bubbles smaller and larger than this critical size experience lift forces of opposite direction, leading to size-dependent radial migration.

The Tomiyama correlation (Tomiyama et al., 2002) is widely used in CFD studies; however, it was developed for unconfined three-dimensional flows and does not explicitly account for geometric confinement. Pseudo-2D experiments consistently report modified lift behavior, including shifts in the critical bubble diameter and changes in force magnitude, indicating that geometric confinement introduces substantial uncertainty in applying Tomiyama lift under shallow-geometry conditions (Ziegenhein et al., 2018; Ziegenhein and Lucas, 2019).

Despite these limitations, several CFD-PBM studies have demonstrated that Tomiyama lift can still yield adequate predictions when combined with suitable turbulence and dispersion closures, particularly at moderate bubble sizes and low gas holdups (Pfleger and Becker, 2001). The broader simulation literature reflects variability: Some studies omit lift altogether (Borchers and Eigenberger, 2004), while others report improved accuracy when it is included for small bubbles (Joshi, 2001; McClure et al., 2014) or for systems with wide bubble-size distributions (Liu et al., 2019). High-resolution measurements (Ziegenhein and Lucas, 2019; Hessenkemper et al., 2021) confirm that lift becomes essential whenever the BSD spans the critical diameter where lift reversal occurs.

Given this strong system dependence, particularly under pseudo-2D confinement, the present work evaluates cases both with and without lift to assess its influence.

2.5. Population Balance Modeling

In this study, the BSD was incorporated into the hydrodynamic framework through a PBM coupled with the Euler-Euler multiphase approach. Each bubble was described by external spatial coordinates x (its position in the flow) and internal coordinates r (intrinsic properties such as volume or characteristic length). Fig. 2 illustrates this concept schematically for two instants of time.

The PBM is expressed in terms of the number density function $n(\boldsymbol{X}, \boldsymbol{R},$

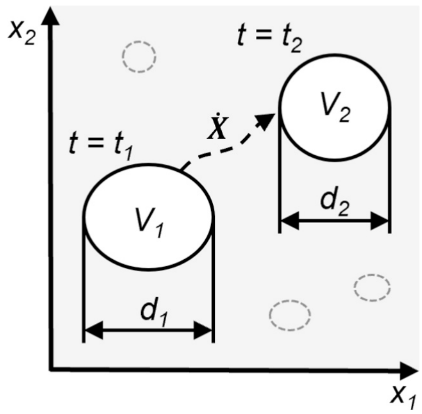

Fig. 2. Conceptual representation of bubble dynamics in the population balance model, showing external spatial coordinates (x_1, x_2) and internal descriptors (bubble volume V, diameter d) at two different time instants t_1 and t_2.

t), where $\boldsymbol{X}$ are external and $\boldsymbol{R}$ internal coordinates. The terms $\dot{\boldsymbol{X}}$ and $\dot{\boldsymbol{R}}$ denote the convective velocities in external and internal coordinate space, respectively. Bubble transport and transformation are represented by convection in both coordinate spaces and by a source term S, which accounts for coalescence and breakage (Eq. (13) (Ramkrishna, 2000):

$$\frac{\partial n}{\partial t} + \nabla_{\boldsymbol{X}} \bullet (\dot{\boldsymbol{X}} n) + \nabla_{\boldsymbol{R}} \bullet (\dot{\boldsymbol{R}} n) = S \tag{13}$$

For practical CFD coupling, the bubble diameter d was used as a single internal coordinate. This reduced the PBM to (Eq. (14) (Hlawitschka et al., 2016; Marchisio and Fox, 2007):

$$\frac{\partial n(d, \boldsymbol{x}, t)}{\partial t} + \nabla_{\boldsymbol{X}} \bullet \left(\boldsymbol{u}_g \, n(d, \boldsymbol{x}, t) \right) = S(d, \boldsymbol{x}, t) \tag{14}$$

In population-resolved multifluid simulations, PBM source terms redistribute number density across size classes, while momentum exchange is resolved separately for each bubble population through distinct Eulerian gas fields.

The net source term $S(d, \boldsymbol{x}, t)$ consists of birth (B) and death (D) contributions associated with both breakage (b) and coalescence (c) processes (Eq. (15), reflecting the redistribution of bubbles between size classes within the BSD:

$$S(d, \boldsymbol{x}, t) = B_b(d, \boldsymbol{x}, t) - D_b(d, \boldsymbol{x}, t) + B_c(d, \boldsymbol{x}, t) - D_c(d, \boldsymbol{x}, t) \tag{15}$$

Following Sanyal et al. (Sanyal et al., 2005) and Hlawitschka (Hlawitschka, 2013), these terms are defined as (Eqs. (16)–(19):

$$B_b(d, \boldsymbol{x}, t) = \int_d^{\infty} g(d') \beta(d|d') n(d', \boldsymbol{x}, t) \, \mathrm{d}d' \tag{16}$$

$$D_b(d, \boldsymbol{x}, t) = g(d) n(d, \boldsymbol{x}, t) \tag{17}$$

$$B_c(d, \boldsymbol{x}, t) = \frac{1}{2} \int_0^d h\left(d', (d^3 - d'^3)^{\frac{1}{3}}\right) n(d', \boldsymbol{x}, t) \, n\left((d^3 - d'^3)^{\frac{1}{3}}, \boldsymbol{x}, t\right) \frac{d^2}{(d^3 - d'^3)^{\frac{2}{3}}} \, \mathrm{d}d' \tag{18}$$

$$D_c(d, \boldsymbol{x}, t) = n(d, \boldsymbol{x}, t) \int_0^{\infty} h(d, d') n(d', \boldsymbol{x}, t) \, \mathrm{d}d' \tag{19}$$

In the breakage terms, d' denotes the parent bubble diameter and d the daughter diameter resulting from breakup. The breakage frequency $g(\cdot)$ specifies the breakup rate of bubbles of a given diameter, while $\beta(d|d')$ denotes the conditional daughter-size distribution generated from a parent bubble of diameter d'.

In the coalescence terms, d denotes the diameter of the product bubble formed by the merging of two parent bubbles with diameters d' and $d'' = (d^3 - d'^3)^{1/3}$ under the assumption of volume conservation. The function $h(d, d')$ represents the coalescence rate between bubbles of diameters d and d'.

2.5.1. Breakage and Coalescence Model Closure

To close the PBM source terms, specific constitutive models for bubble breakage and coalescence were employed. The development and physical foundations of commonly used breakup and coalescence kernels are comprehensively reviewed by Liao and Lucas (Liao and Lucas, 2009; Liao and Lucas, 2010), who discuss their theoretical background and applicability ranges.

Based on these established formulations, the kernel models applied in the present study are specified in the following sections. To date, no generally accepted breakup or coalescence kernels explicitly accounting for geometric confinement have been established for Euler-Euler CFD-PBM simulations of pseudo-2D bubbly flows. Consequently, the present study employs established baseline closures to ensure a consistent assessment of PBM formulation effects.

2.5.1.1. Breakage Kernel. Bubble breakage is modeled using the breakage frequency $g(d)$ and the daughter size distribution $\beta(d|d')$ proposed by Laakkonen et al. (Laakkonen et al., 2006). Although originally developed for liquid-liquid dispersions in stirred tanks (Narsimhan et al., 1979; Alopaeus et al., 2002), this formulation has been successfully applied to gas-liquid systems as well (Artz et al., 2018; Buffo et al., 2013; Hlawitschka et al., 2016). The physical basis of the model lies in turbulence-induced rupture mechanisms that are common to both reactor types.

The corresponding breakage frequency is given by (Eq. (20):

$$g(d) = C_1 \, \varepsilon^{\frac{1}{3}} erfc\left(\sqrt{C_2 \frac{\sigma}{\rho_l \varepsilon^{\frac{2}{3}} d^{\frac{5}{3}}} + C_3 \frac{\eta_l}{\sqrt{\rho_l \rho_g} \, \varepsilon^{\frac{2}{3}} d^{\frac{4}{3}}}} \right) \tag{20}$$

Here, the coefficients $C_2 = 0.04$ and $C_3 = 0.01$ arise from turbulence-based scaling arguments, while the empirical parameter $C_1 = 4$ has been validated for air-water dispersions, supporting the applicability of the model to bubble column flows (Petitti et al., 2010).

The corresponding daughter size distribution $\beta(d|d')$, describing binary fragmentation, is given by a beta distribution (Eq. (21) (Laakkonen et al., 2006):

$$\beta(d|d') = 180 \left(\frac{d^2}{d'^3} \right) \left(\frac{d^3}{d'^3} \right)^2 \left(1 - \frac{d^2}{d'^3} \right)^2 \tag{21}$$

The Laakkonen breakup model expresses the breakup probability as a function of the local turbulent energy dissipation rate ε and accounts for inertial and viscous stabilizing effects through the error function. Since ε is supplied by the URANS turbulence closure, breakup predictions inherently reflect the limitations of time-averaged turbulence modeling.

While the model neglects effects such as bubble shape deformation, turbulence anisotropy, confinement influences, and non-binary breakup, it remains one of the most widely used breakup formulations in Euler-Euler CFD-PBM simulations due to its physical transparency and numerical robustness.

More mechanistic breakup kernels, such as the model proposed by Luo and Svendsen (Luo and Svendsen, 1996), describe interactions between turbulent eddies and bubble interfaces by integrating over the turbulent eddy spectrum. Although physically detailed, these formulations are highly sensitive to local turbulence dissipation rates and prone to numerical stiffness in URANS-based Euler-Euler simulations; their applicability to pseudo-2D confined geometries has not been systematically validated, and their strong dependence on local dissipation suggests limited robustness under shallow confinement (Marchisio and Fox, 2013; Buffo et al., 2013).

In contrast, classical energy-based kernels, including the Coulaloglou-Tavlarides model (Coulaloglou and Tavlarides, 1977), rely on simplified breakup criteria and global or turbulence-averaged scales. While numerically robust, such approaches are less capable of capturing the pronounced spatial inhomogeneities characteristic of heterogeneous and confined bubble columns. More advanced formulations (e.g., Martínez-Bazán (Martínez-Bazán et al., 1999), Lehr (Lehr et al., 2002), or DNS/LES-derived models) incorporate additional physical mechanisms such as intermittency or bubble deformation. While these approaches offer increased physical fidelity, their predictive capability often relies on turbulence characteristics that are only coarsely represented in URANS closures, and their applicability to air-water pseudo-2D systems remains unclear.

Against this background, the Laakkonen kernel represents a practical compromise between physical fidelity and numerical robustness. Its formulation retains sensitivity to locally resolved turbulence dissipation while remaining compatible with URANS-based Euler-Euler-PBM simulations, providing a reliable and computationally stable basis for the present study.

2.5.1.2. Coalescence Kernel. The coalescence rate $h(d, d')$ is modeled as the product of a collision frequency $h_0(d, d')$ and a coalescence efficiency $\lambda(d, d')$ (Eq. (22) (Besagni et al., 2018):

$$h(d, d') = h_0(d, d')\lambda(d, d') \tag{22}$$

The collision frequency describes the number of bubble encounters per unit time and is commonly modeled analogously to molecular collisions in kinetic gas theory. In bubbly flows, collisions are predominantly driven by turbulent eddies (Liao and Lucas, 2010). The collision frequency due to turbulence is defined as (Eq. (23):

$$h_0(d, d') = u_{rel}S_{12} \tag{23}$$

The relative approach velocity u_{rel} and the collision cross-section S_{12} are calculated according to Prince and Blanch (Prince and Blanch, 1990) (Eqs. (24) and (25):

$$S_{12} = \frac{\pi}{4}(d + d')^2 \tag{24}$$

$$u_{rel} = \sqrt{2}\varepsilon^{\frac{1}{3}}\sqrt{d^{\frac{2}{3}} + d'^{\frac{2}{3}}} \tag{25}$$

Inserting (24) and (25) into (23) yields the full turbulence-driven collision rate (Eq. (26):

$$h_0(d, d') = \sqrt{2}\ \frac{\pi}{4}(d + d')^2\varepsilon^{\frac{1}{3}}\sqrt{d^{\frac{2}{3}} + d'^{\frac{2}{3}}} \tag{26}$$

Once two bubbles collide, different outcomes are possible (coalescence, rebound, or breakup). The probability of coalescence is expressed *via* the efficiency $\lambda(d, d')$. The most widely used approach is the film drainage model, which assumes that a thin liquid film forms upon collision. Coalescence occurs once the film drains and ruptures within the bubble contact time. The efficiency is defined as (Eq. (27) (Coulaloglou and Tavlarides, 1977):

$$\lambda(d, d') = \exp\left(-\frac{t_D}{\tau}\right) \tag{27}$$

where t_D donates the film drainage time and τ the contact time.

Following Prince and Blanch (Prince and Blanch, 1990), the film drainage process is characterized using the equivalent bubble diameter d_{eq} (Eq. (28):

$$d_{eq} = \left(\frac{1}{d} + \frac{1}{d'}\right)^{-1} \tag{28}$$

Yielding the film drainage time t_D (Eq. (29) and the contact time τ (Eq. (30):

$$t_D = \left(\frac{\rho_l d_{eq}^3}{16\,\sigma}\right)^{\frac{1}{2}} \ln\left(\frac{h_f}{h_{crit}}\right) \tag{29}$$

$$\tau = \frac{d_{eq}^{\frac{2}{3}}}{\varepsilon^{\frac{1}{3}}} \tag{30}$$

Here, $h_f = \exp(-4)$, $h_{crit} = \exp(-8)$ are dimensionless film-thickness parameters representing the initial film thickness after collision and the critical rupture thickness, respectively.

Substituting (29) and (30) into (27) yields the final expression for the coalescence efficiency (Eq. (31):

$$\lambda(d, d') = \exp\left(-\frac{\rho_F^{\frac{1}{2}}\varepsilon^{\frac{1}{3}}d_{eq}^{\frac{5}{6}}}{4\sigma^{\frac{1}{2}}}\ln\left(\frac{h_f}{h_{crit}}\right)\right) \tag{31}$$

The Prince and Blanch (Prince and Blanch, 1990) kernel is widely used in CFD-PBM simulations, because it provides a physically intuitive description of turbulent collision dynamics and film drainage, while exhibiting strong numerical robustness and reduced sensitivity to local fluctuations in ε. Its underlying assumptions – spherical bubbles, mobile interfaces, negligible surfactant effects, and no explicit confinement corrections – are like those of most coalescence models used in Euler-Euler frameworks.

Alternative coalescence formulations primarily differ in how turbulence-interface interactions are represented. The energy-based model of Luo (Luo and Coalescence, , 1995), for example, compares turbulent eddy kinetic energy with film-stabilizing interfacial energy. Although more mechanistic, its pronounced dependence on local turbulence dissipation renders it susceptible to numerical stiffness in URANS-based Euler-Euler simulations and may limit its robustness under weakly turbulent or confined pseudo-2D conditions. The velocity-threshold model of Lehr et al. (Lehr et al., 2002); in contrast, assumes rebound above a critical approach velocity and yields a simple empirical expression for λ. While numerically robust and often comparable to the Prince and Blanch kernel at moderate turbulence levels, it lacks a direct physical link to film-drainage-controlled coalescence. These alternative formulations emphasize different physical mechanisms and may exhibit different sensitivities to the local turbulence field and flow conditions.

Against this backdrop, the Prince and Blanch kernel provides a balanced and practically reliable choice for the present pseudo-2D configuration. It combines a physically interpretable film-drainage mechanism with good numerical robustness and has been widely applied in Euler-Euler CFD-PBM simulations of bubbly flows. Furthermore, its moderate sensitivity to local dissipation-rate fluctuations makes it well suited for coupling with URANS-based turbulence closures. The model therefore provides a consistent baseline coalescence closure for the systematic PBM comparison conducted in this work.

2.5.2. Bubble Size Representation

While the breakup and coalescence kernels define the transformation of bubbles in size space, the BSD must additionally be represented in a numerically tractable form for coupling with the CFD framework. Within population balance modeling, this requires a suitable approximation of the continuous number density function.

A central coupling quantity between the PBM and the hydrodynamic model is the Sauter mean diameter d_{32}, which relates the total bubble volume to its surface area (Eq. (32) and is directly used in interfacial force and mass-transfer correlations (Pacek et al., 1998):

$$d_{32} = \frac{\sum_i n_i d_i^3}{\sum_i n_i d_i^2} \quad (32)$$

Two commonly used approaches to represent the BSD in CFD-PBM simulations are the discrete class method and the Method-of-Moments.

2.5.2.1. Discrete Class Method. In the discrete class method, the continuous bubble-size distribution is subdivided into finite intervals (classes). The class-wise number density $N_i(\boldsymbol{x}, t)$ represents the number of bubbles per unit volume within size interval i and is obtained by integrating the continuous number density function over the corresponding class boundaries. For each size class i, this quantity is computed by integrating the distribution between the class boundaries $d_{i-0.5}$ and $d_{i+0.5}$ (Eq. (33) (Khan, 2014; Kumar and Ramkrishna, 1996):

$$N_i(\boldsymbol{x}, t) = \int_{d_{i-0.5}}^{d_{i+0.5}} n(d, \boldsymbol{x}, t)\, \mathrm{d}d \quad (33)$$

In this work, two variants were implemented. The single-population version employed nine classes covering diameters from 1 to 10 mm, using uniform 1 mm class widths defined as half-open intervals [1–2), [2–3), …, (Wang and Wang, 2017; Liao and Lucas, 2009) mm. The modeled bubble size range was limited to diameters up to 10 mm, as larger bubbles tend to exhibit increased deformation and instability (Clift et al., 2005), and may therefore be associated with increased modeling uncertainty in Euler-Euler CFD-PBM approaches. The class fractions were initialized from the prescribed log-normal inlet bubble-size distribution, ensuring consistency with the corresponding moment-based formulations.

In the population-resolved multifluid variant, these nine classes were grouped into three bubble populations representing small, medium, and large bubbles. Each bubble population was implemented as a separate Eulerian gas field to allow distinct momentum balances and size-dependent slip velocities. The intervals [1–2), [2–3), and [3–4) mm were assigned to the small-bubble population; [4–5), [5–6), and [6–7) mm to the medium-bubble population; and [7–8), [8–9), and (Wang and Wang, 2017; Liao and Lucas, 2009) mm to the large-bubble population. This grouping provides a balanced partition of the distribution while maintaining numerical stability. The resolution was selected as a compromise between computational cost and model fidelity and was found adequate for capturing the experimentally observed bubble size range, although finer discretization would improve higher-order statistics.

2.5.2.2. Statistical Method-of-Moments. Alternatively, BSDs were characterized through the statistical moments of the gas phase (Khan, 2014). For spherical bubbles, the zeroth moment M_0 is proportional to the total bubble number, the first moment M_1 to a diameter-weighted measure of bubble size, the second moment M_2 to the total interfacial area, and the third moment M_3 to the total bubble volume.

In general, the j-th moment of the number density function $n(d, \boldsymbol{x}, t)$ is defined as (Eq. (34) (Sanyal et al., 2005; Kumar and Ramkrishna, 1996):

$$M_j(\boldsymbol{x}, t) = \int_0^\infty n(d, \boldsymbol{x}, t) d^j \mathrm{d}d \quad (34)$$

In this study, the first four moments M_0 to M_3 were solved. Instead of resolving the BSD explicitly, transport equations for the moments were considered (Eq. (35) (L. Gemello, Modelling of the Hydrodynamics of Bubble Columns Using a Two-Fluid Model Coupled with a Population Balance Approach, PhD thesis, Université Claude Bernard Lyon 1, Lyon, France and Politecnico di Torino, Turin, Italy, 2018; Marchisio and Fox, 2013):

$$\frac{\partial M_j}{\partial t} + \nabla \bullet (\boldsymbol{u}_g M_j) = S_j \quad (35)$$

To close the system, quadrature-based methods were applied. In the single-population variant, the quadrature Method-of-Moments (QMoM) was used, approximating the integrals by a finite set of representative bubble sizes d_i (abscissas) and corresponding weights w_i (Eq. (36) (Hlawitschka et al., 2016; Marchisio and Fox, 2007):

$$M_j(\boldsymbol{x}, t) = \int_0^\infty n(d, \boldsymbol{x}, t) d^j\, \mathrm{d}d \approx \sum_{i=1}^{N} w_i d_i^j \quad (36)$$

The first four moments (M_0 to M_3) were initialized from the same prescribed log-normal inlet bubble-size distribution used for the class-based formulations. Quadrature abscissas and weights were subsequently obtained through moment inversion.

In the population-resolved multifluid configuration, the direct quadrature Method-of-Moments (DQMoM) available in ANSYS Fluent was applied (Anderson, 2002). In contrast to the conventional QMoM formulation, where all quadrature nodes share a common velocity field, DQMoM associates the quadrature nodes with separate dispersed-phase fields, thereby enabling size-dependent hydrodynamic behavior and particle segregation.

In the present implementation, three dispersed gas populations were employed, consistent with the multifluid framework used throughout this study. The first four moments were transported, while the corresponding quadrature-node diameters and weights were initialized from the prescribed inlet moments using moment inversion and subsequently evolved through the DQMoM transport equations.

The hydrodynamic coupling between the PBM and the Euler-Euler framework is achieved through the population-specific gas phases. Consequently, the different dispersed populations may develop different slip velocities and interfacial force balances, allowing size-dependent transport effects to be represented without explicit discretization of the bubble-size spectrum.

This formulation facilitates coupling to multifluid frameworks, where size-dependent slip velocities and momentum balances must be represented explicitly.

2.5.2.3. Conceptual Comparison of PBM Approaches. The two PBM formulations offer complementary strengths. The class method resolves bubble sizes explicitly during runtime and thus provides direct access to the BSD, which facilitates comparison with experimental distributions. Its computational cost increases with the number of discretized size classes, and coarse resolution may reduce accuracy. Moment-based approaches represent the BSD through a limited set of statistical moments and therefore require fewer transport equations. Their main limitations are the lack of an explicit BSD without reconstruction and potential sensitivity to strong bimodality or pronounced distribution-shape variations.

In the single-population configuration, differences in computational effort originate from the additional PBM transport equations and source-term evaluations. The class method solves one scalar equation per size class (nine in total), whereas the single-population Method-of-Moments (QMoM) transports four moment equations. For otherwise identical hydrodynamic settings, this results in lower CPU demand for the moment-based formulation.

In population-resolved multifluid models, computational cost additionally scales with the number of Eulerian gas phases, since each population requires its own continuity and momentum equations. In the class-based formulation, class fractions are distributed across the gas phases, while the multifluid moment-based model employs DQMoM and transports quadrature nodes and weights per population. The dominant cost increase in multifluid simulations therefore arises from the additional hydrodynamic transport equations, whereas the PBM-related contribution depends on the chosen size representation.

Fig. 3 illustrates the conceptual differences between the two approaches. The continuous number-based density function (solid line) may be discretized into piecewise-constant intervals (bars) in the class

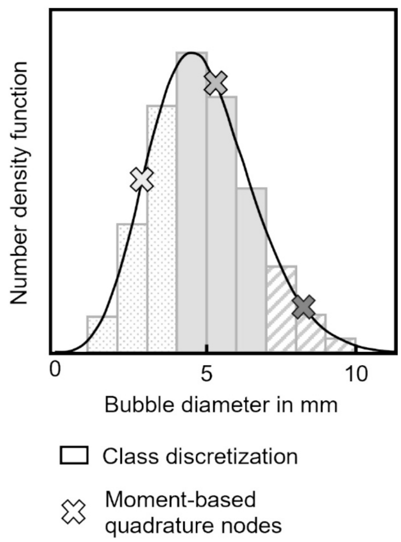

Fig. 3. Representation of the BSD by different PBM approaches: continuous number-based density function (solid line), discrete class method (bars), and quadrature nodes of the Method-of-Moments (markers).

method or approximated by a small number of quadrature nodes (markers) in the Method-of-Moments. Considering both formulations in parallel enables a systematic comparison of discrete and moment-based representations and clarifies their respective structural suitability for describing size-dependent bubble dynamics in polydisperse gas-liquid flows.

2.6. Grid and Time-Step Independence Study

A grid and time-step independence study was performed to ensure numerical robustness of the simulations. Three structured hexahedral meshes containing 2,400, 4,500, and 9,625 cells were investigated. Since the Euler-Euler framework employs volume-averaged conservation equations, the mesh resolution was selected to remain on the order of the characteristic bubble diameter rather than substantially below it. The minimum cell sizes of the investigated meshes ranged from 5.7 to 8.0 mm and were therefore comparable to the predicted bubble diameters.

Temporal resolution was assessed using time steps of 0.05, 0.025, and 0.01 s. Based on the minimum cell size and a characteristic liquid velocity of 0.3 m s^{-1} reported for comparable pseudo-2D bubble columns, a CFL-based stability limit of approximately 0.03 s was estimated. In addition to overall gas holdup, the plume oscillation period was evaluated as a transient indicator of discretization sensitivity.

The medium mesh (4,500 cells) and a time step of 0.025 s yielded stable solutions, while further refinement produced only minor changes in the predicted gas holdup and plume oscillation period at substantially higher computational cost. This configuration therefore provided a suitable compromise between numerical accuracy and computational efficiency and was adopted for all subsequent simulations. Further refinement increased computational demand considerably without altering the predicted flow regime or the overall hydrodynamic trends. A detailed description of the discretization analysis is provided in Section S2 of the Supplementary Information.

3. CFD-PBM Results and Model Assessment

The CFD-PBM simulations of the pseudo-2D bubble column were compared with experimental data, focusing on model accuracy, computational cost, and the ability to capture size-dependent hydrodynamics. The models investigated here differed in the applied population balance method, the degree of population resolution, and the inclusion of the lateral lift force. Each configuration is denoted as Method+Phases-Lift, where:

- Method = C (class method) or M (Method-of-Moments)
- Populations = 1 (single-population representation) or 3 (population-resolved multifluid representation)
- Lift = LL (with lateral lift force) or omitted (no lift force)

In the population-resolved configurations, three bubble populations are modeled separately within the multifluid framework. The single-population configurations, in contrast, describe the dispersed phase by a common momentum balance for all bubble sizes.

Model performance is first evaluated based on the global quantities gas holdup and Sauter mean diameter. The assessment is then extended by considering the plume oscillation period (POP) as a transient metric of large-scale plume dynamics, followed by analyses of time-averaged local gas-holdup distributions and predicted BSD to evaluate flow structures and size-dependent segregation behavior.

Numerical values underlying the quantitative results discussed in this section are provided in Section S3.1 of the Supplementary Information.

3.1. Overall Gas Holdup

The overall gas holdup in the bubble column, defined as the volume-averaged gas holdup over the entire column volume, is shown in Fig. 4 for (a) the class method and (b) the Method-of-Moments, together with experimental data from Díaz et al. (Díaz et al., 2008).

In the absence of the lateral lift force, both single-population models correctly reproduce the increase in gas holdup with superficial gas velocity, but tend to underpredict its magnitude at low and intermediate velocities. In this regime, relative deviations reach values of up to approximately 25 % for both PBM approaches. These relatively large percentage deviations arise from the small absolute values of the gas holdup at these conditions. At the highest superficial gas velocity ($u_{s,g,3}$= 21.3 mm s^{-1}), the agreement improves, and deviations decrease to below 10 % for both models.

Population-resolved multifluid extensions yield nearly identical results to the corresponding single-population models, indicating that increased population resolution does not significantly affect the prediction of the volume-averaged gas holdup.

Including the lateral lift force consistently decreases the predicted gas holdup. This effect is minor in the class method, where accuracy improves at higher velocities, matching the experiment at $u_{s,g,3}$= 21.3 mm s^{-1} within a relative deviation of approximately 1 %. In contrast, the Method-of-Moments shows a stronger reduction, leading to larger discrepancies. Consequently, while lift inclusion is neutral to slightly beneficial for the class method, it is not recommended for the Method-of-Moments approach.

3.2. Overall Sauter Mean Diameter

Fig. 5 compares the predicted overall Sauter mean diameters from the class method (a) and the Method-of-Moments (b) with the experimental reference data of Díaz et al. (Díaz et al., 2008).

The single-population class method reproduces experimental Sauter mean diameters with good accuracy and relative deviations below 8 % across all conditions. In contrast, the single-population Method-of-Moments matches experiments at low gas velocities but overpredicts bubble sizes at higher velocities, with deviations exceeding 40 % at $u_{s,g,2}$= 11.9 mm s^{-1}. Nevertheless, its relatively low computational demand and acceptable performance for overall quantities at low velocities indicate that it may remain applicable in scenarios where accurate resolution of size-dependent hydrodynamics is not required. Introducing a population-resolved multifluid formulation reduces predicted Sauter

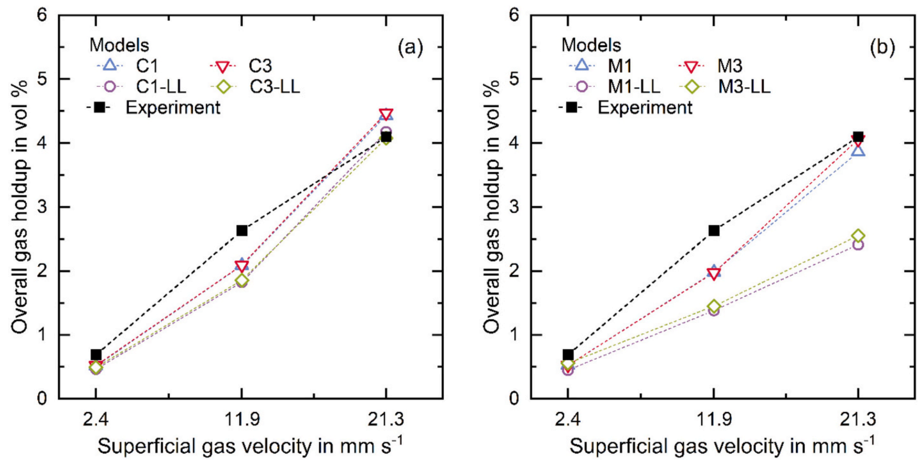

Fig. 4. Predicted overall gas holdup as a function of superficial gas velocity for (a) the class method and (b) the Method-of-Moments. Simulations (open symbols) are compared to experimental data (squares). Even though both methods identify the trend, the class method shows closer agreement at higher velocities.

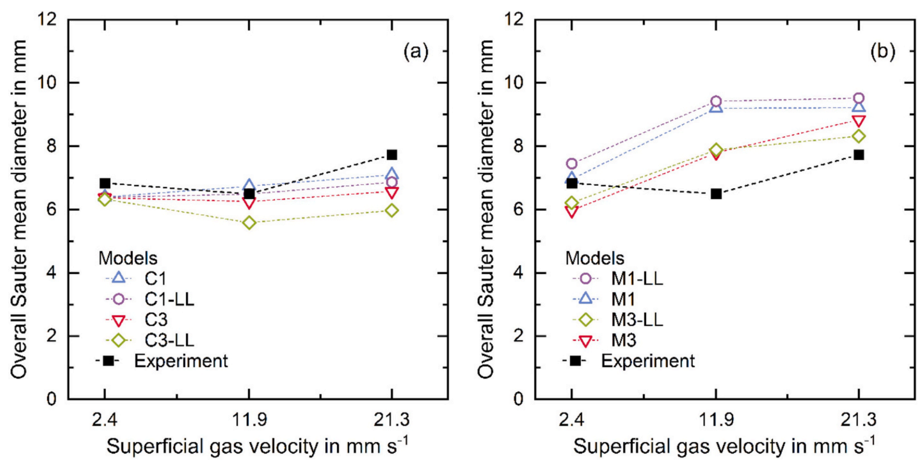

Fig. 5. Predicted overall Sauter mean diameter as a function of superficial gas velocity for (a) the class method and (b) the Method-of-Moments, compared to the experimental data. The class method shows good agreement across the investigated velocity range, whereas the Method-of-Moments predicts larger mean diameters, particularly at higher superficial gas velocities.

mean diameters, as the additional momentum balances allow partial differentiation of slip velocities between populations. For the class method, this does not significantly improve agreement, whereas for the Method-of-Moments it reduces the tendency to overpredict bubble sizes and lowers deviations to around 20 %.

For the class method, the inclusion of the lateral lift force has only a

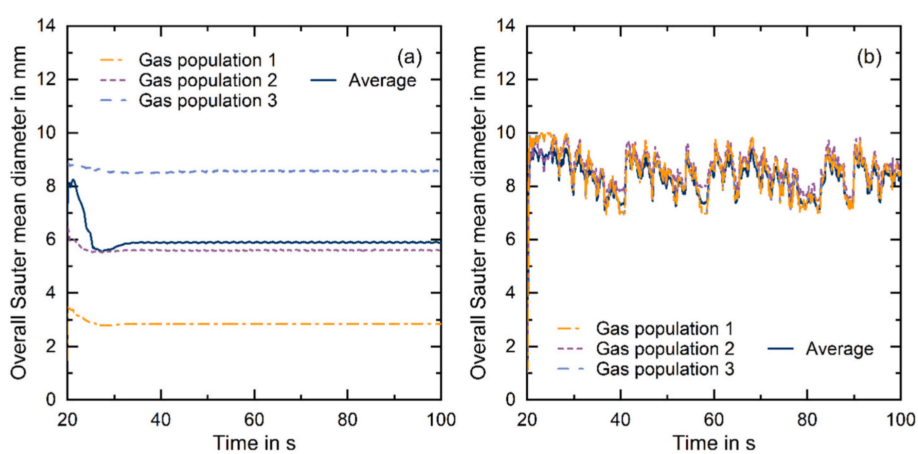

Fig. 6. Temporal evolution of the Sauter mean diameter at$u_{s,g,3}$ = 21.3 mm s^{-1} in population-resolved multifluid simulations. (a) Class method (C3): distinct size classes persist with moderate redistribution. (b) Method-of-Moments (M3): the Sauter mean diameters of all bubble phases converge over time, indicating insufficient coupling between bubble size and hydrodynamics.

minor influence on the predicted Sauter mean diameter, although it tends to slightly reduce agreement with the experimental data, particularly in the population-resolved configuration. For the Method-of-Moments, the impact of the lift force is less consistent: in some cases predictions improve marginally, whereas in others deviations increase, resulting in no systematic enhancement of model accuracy.

Fig. 6 illustrates the temporal evolution of the Sauter mean diameter for the population-resolved class method (a) and the population-resolved Method-of-Moments (b).

In the Method-of-Moments, the Sauter mean diameters of the individual bubble populations rapidly converge despite distinct initializations and remain nearly identical throughout the simulation. This convergence implies insufficient coupling between bubble size and hydrodynamics, resulting in similar interfacial drag forces and slip velocities across the resolved populations. Consequently, the population-resolved multifluid formulation of the Method-of-Moments offers no clear advantage over the corresponding single-population model.

In contrast, the class method maintains discrete size classes throughout the simulation. Although breakage and coalescence redistribute gas volume fractions among classes, the representative diameter of each class remains confined to its prescribed interval. Persistent size differences between populations therefore lead to distinct drag forces and slip velocities, sustaining size-dependent hydrodynamic differentiation over time. The bounded class intervals also limit the maximum resolvable bubble size, contributing to the comparatively smaller predicted Sauter mean diameters. While this discretization reduces flexibility relative to the Method-of-Moments, it preserves structural size separation within the multifluid framework.

3.3. Plume Oscillation Dynamics

To complement the validation based on overall gas holdup and Sauter mean diameter, the transient plume dynamics were quantitatively assessed using the plume oscillation period (POP). The POP was evaluated at a column height of 0.2 m, corresponding to the central measurement plane where the lateral plume motion was most pronounced. This position corresponds closely to the intermediate measurement location used by Díaz et al. (Díaz et al., 2008) (21.3 cm above the sparger), who further reported that the measured plume oscillation period was largely independent of sensor position within the column. The POP was determined by tracking the lateral position of the maximum gas holdup over time. Individual oscillation periods were obtained from the temporal spacing between successive plume excursions, and the reported POP represents the average of all detected oscillation periods within the evaluation interval. The predicted oscillation periods are compared with the experimental values in Fig. 7.

The experimental data exhibit a pronounced decrease in oscillation period with increasing superficial gas velocity, indicating a transition from slow plume meandering at low gas velocities to faster oscillatory motion at elevated gas rates. This trend is consistently reproduced by all standard PBM formulations, irrespective of whether the class method or the Method-of-Moments is employed. Although quantitative deviations remain, the predicted oscillation periods are of the same order of magnitude as the experimental observations and capture the overall evolution of the transient plume dynamics.

The influence of the lateral lift force is less systematic. While C3-LL remains close to the experimentally observed trend and M1-LL exhibits only minor deviations, C1-LL predicts a substantially increased oscillation period at the intermediate gas velocity. This behavior is not reflected in the experimental data and indicates a pronounced stabilization of the plume motion. A similar, although less pronounced, reversal of the trend is observed for M3-LL at the highest superficial gas velocity. These findings suggest that the employed lift-force formulation can alter the transient plume dynamics under confined conditions and, in specific configurations, lead to an over-stabilization of the plume motion.

Apart from the lift-force-related deviations, the predicted oscillation periods are remarkably similar for the class-based and moment-based PBM formulations. This indicates that the large-scale transient plume dynamics are captured consistently by both approaches and are considerably more sensitive to the interfacial-force formulation than to the selected PBM framework.

Additional analyses of local gas-holdup signals, including a quantitative assessment of plume spreading, are provided in the Supplementary Information (Table S8).

3.4. Local Gas Distribution and Flow Structures

While the POP provides a quantitative measure of the transient lateral plume motion, the gas-holdup fields presented in this section represent time-averaged distributions and therefore characterize the mean flow structure rather than the instantaneous plume dynamics. These spatial gas-holdup distributions enable direct assessment of the predicted flow structures and segregation patterns and were analyzed to evaluate whether the investigated models reproduce the characteristic flow behavior observed in pseudo-2D bubble columns. All configurations reproduce the characteristic transition from a narrow central plume at low gas velocity to a broader and more heterogeneous gas distribution at higher gas velocities, consistent with the flow regimes reported by Díaz et al. (Díaz et al., 2008) and Cachaza et al. (Cachaza

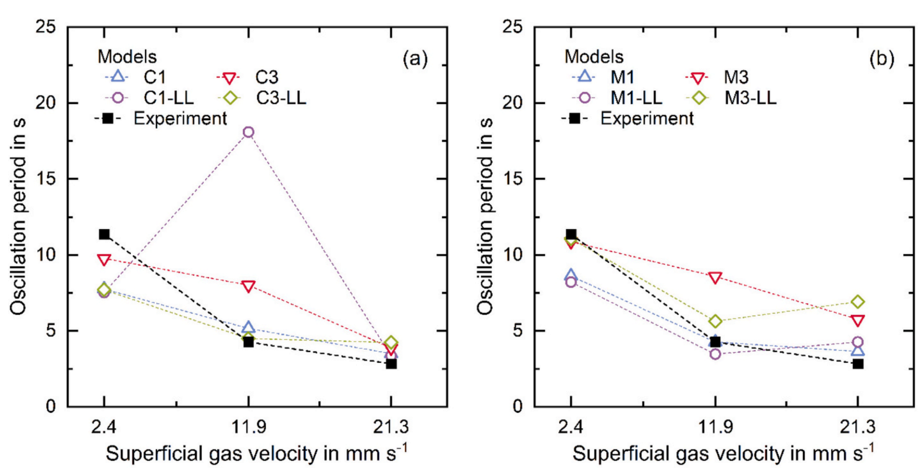

Fig. 7. Average plume oscillation period obtained from local gas-holdup signals as a function of superficial gas velocity for (a) the class method and (b) the Method-of-Moments, compared to experimental data.

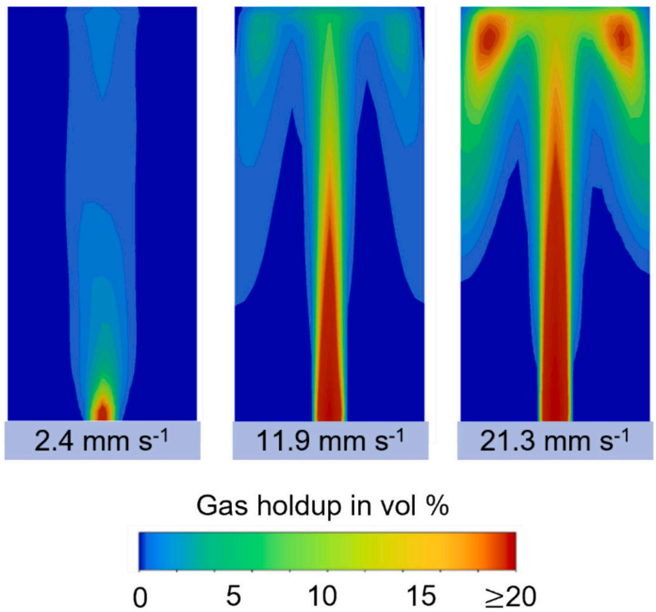

Fig. 8. Time-averaged local gas holdup distribution for the single-population class method (C1) at increasing superficial gas velocities. The local gas holdup distributions are averaged over 40–100 s, after initial transients have decayed. With increasing gas velocity, the spatial gas holdup distribution evolves from a predominantly central plume toward a broader distribution extending into the upper and lateral regions of the column.

et al., 2008).

Fig. 8 shows the time-averaged local gas distribution for the single-population class method (C1) at increasing superficial gas velocities. The averaging procedure suppresses the instantaneous lateral plume oscillation and therefore highlights the mean flow structure.

At low gas velocity ($u_{s,g,1}$= 2.4 mm s^{-1}), the gas phase is concentrated in a predominantly vertical plume above the inlet, extending over a limited lateral region. At intermediate velocity ($u_{s,g,2}$= 11.9 mm s^{-1}), the overall gas distribution becomes more structured, with increased gas presence near the lateral regions of the column. At the highest gas velocity ($u_{s,g,3}$= 21.3 mm s^{-1}), gas holdup extends further into the upper part of the column and into regions away from the plume core, indicating the development of a recirculation-dominated regime.

Comparable regime-dependent changes in the spatial gas holdup distribution were observed across all investigated model configurations; representative examples are shown in Fig. S2 of the Supplementary Information. The resulting plume structures and their evolution with increasing superficial gas velocity are consistent with commonly reported flow patterns in pseudo-2D bubble columns (Díaz et al., 2008).

Fig. 9 compares the time-averaged local gas holdup distributions of the single-population and the corresponding population-resolved multifluid simulations at $u_{s,g,3}$= 21.3 mm s^{-1}. In each row, the single-population result is shown on the left, while the corresponding population-resolved multifluid simulation is shown on the right. In the multifluid cases, the three resolved bubble populations (labeled 1–3) are displayed separately.

For the class method (a and c), the population-resolved formulation produces clearly differentiated spatial distributions among the bubble populations. The populations representing smaller bubbles (1 and 2) extend further toward the lateral and upper regions, whereas the population representing larger bubbles (3) remains concentrated predominantly in the column core. This spatial separation reflects size-dependent hydrodynamic responses under confined conditions and is consistent with experimentally reported segregation patterns in pseudo-2D bubble columns (Díaz et al., 2008).

By contrast, the population-resolved Method-of-Moments

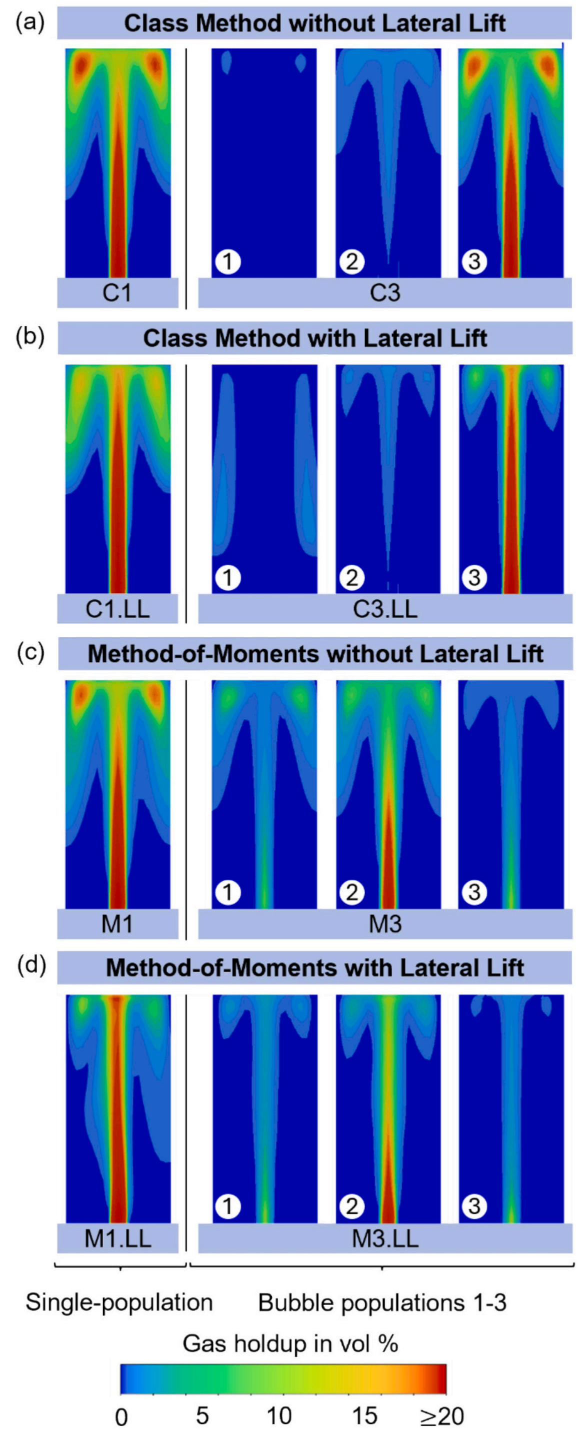

Fig. 9. Time-averaged local gas distributions at$u_{s,g,3}$ = 21.3 mm s^{-1}. In each row, the single-population simulation (left) is compared with the corresponding population-resolved simulation (right), where the three bubble populations are shown separately. The class method (a and b) exhibits distinct spatial structuring between populations, whereas the Method-of-Moments formulation (c and d) shows largely similar plume structures across all populations.

formulation (c and d) does not produce a comparably distinct spatial separation. Instead, all populations follow the same dominant plume structure, indicating limited size-conditioned differentiation of the flow field. This homogenized spatial behavior is consistent with the convergence of representative bubble sizes observed in Section 3.2. At the same time, the POP analysis demonstrated that both PBM methods reproduce the large-scale plume motion with comparable accuracy. The differences therefore primarily concern the representation of population-level segregation rather than the overall plume dynamics.

In both modeling approaches, activating lift modifies the radial distribution by shifting gas volume fractions toward the column center, consistent with the diameter-dependent lift formulation employed. Under steady operating conditions and fixed superficial gas velocity, the overall gas holdup scales with the mean residence time of the dispersed phase. A stronger central plume concentrates bubbles in the high-velocity core region and reduces their residence in lateral and recirculation zones. This redistribution is therefore expected to decrease the effective gas residence time and is consistent with the reduced overall gas holdup observed in Fig. 4.

3.5. Bubble Size Distributions

The class method provides direct access to the bubble size distribution (BSD), which is analyzed to evaluate size-dependent volume redistribution. Fig. 10 compares the normalized BSDs for the single-population (C1) and population-resolved multifluid (C3) configurations at $u_{s,g,3} = 21.3$ mm s^{-1}, evaluated as plane- and time-averaged distributions on a horizontal cross-section at a height of 0.3 m. Corresponding comparisons at lower superficial gas velocities are provided in Figs. S3 and S4 of the Supplementary Information. Height-resolved BSDs illustrating the vertical evolution of the size spectrum are shown in Figs. S5 and S6.

In the single-population configuration (C1), the BSD remains broadly distributed across the resolved diameter range and does not exhibit a systematic migration of gas volume toward a specific size interval. Including the lateral lift force alters the distribution only marginally. Within a shared momentum balance, breakup and coalescence redistribute volume among classes but do not generate a directional shift toward particular diameter ranges.

In contrast, the multifluid configuration (C3) exhibits a clear redistribution of gas volume toward the largest resolved class. This shift reflects a sustained net transfer of volume toward larger diameter classes within the resolved spectrum under population-resolved momentum balances. The lift force amplifies the accumulation in the largest class but does not initiate the redistribution.

A distinct accumulation occurs at the imposed upper class boundary (10 mm). As shown in Fig. S7 of the Supplementary Information, extending the discretization to 13 mm shifts the accumulation toward the new upper boundary, demonstrating that the observed maximum diameter is governed by the imposed size truncation rather than by an independently resolved physical growth limit. This truncation effect primarily influences bubble-size metrics. Extending the admissible size range led to an increase in the predicted Sauter mean diameter, indicating that this quantity is sensitive to the selected upper size limit. In contrast, the overall gas holdup changes only moderately, suggesting that bulk hydrodynamic quantities are less affected by the truncation than size-based metrics.

Consequently, the reported Sauter mean diameters should be interpreted in the context of the imposed size range. Nevertheless, the qualitative trends in bubble-size redistribution, hydrodynamic population resolution, and size-dependent segregation remained consistent across the investigated size-range variations, indicating that the comparative assessment of PBM formulation effects is robust with respect to the selected truncation limit.

To further assess the influence of the breakup-coalescence balance, selected kernel parameters were systematically scaled (Fig. S7). The coalescence rate (Prince & Blanch) was reduced by 50 %, and the Laakkonen breakup frequency was increased by factors of two and four. Reducing the coalescence rate did not suppress the accumulation at the upper class boundary. Doubling the breakup frequency had only limited impact, whereas increasing it by a factor of four eliminated the upper-class peak and redistributed volume toward intermediate diameters. The corresponding global quantities are summarized in Table S5.

Overall, the BSD analysis confirms that multifluid modeling enables sustained size redistribution, whereas the upper-bound accumulation reflects a structural consequence of the imposed size truncation and the selected breakup-coalescence balance rather than an independently resolved physical size limit.

3.6. Numerical Performance

Computational cost differed systematically between the investigated model variants and remained nearly constant across the investigated range of superficial gas velocities.

In the single-population configuration, the class model (C1) required approximately 30–35 % more CPU time than the corresponding Method-of-Moments model (M1).

Introducing population-resolved multifluid modeling increased runtime substantially for both formulations. Relative to their single-population counterparts, M3 required approximately 100–105 % more CPU time than M1, while C3 required about 120 % more CPU time than C1.

Within the multifluid framework, the class-based model (C3) remained consistently 40–45 % more expensive than the Method-of-Moments variant (M3).

The resulting ranking of computational cost was therefore: M1 $<$ C1 $<$ M3 $<$ C3.

The inclusion of the lateral lift force had no measurable impact on runtime. The reported values correspond to the present discretization

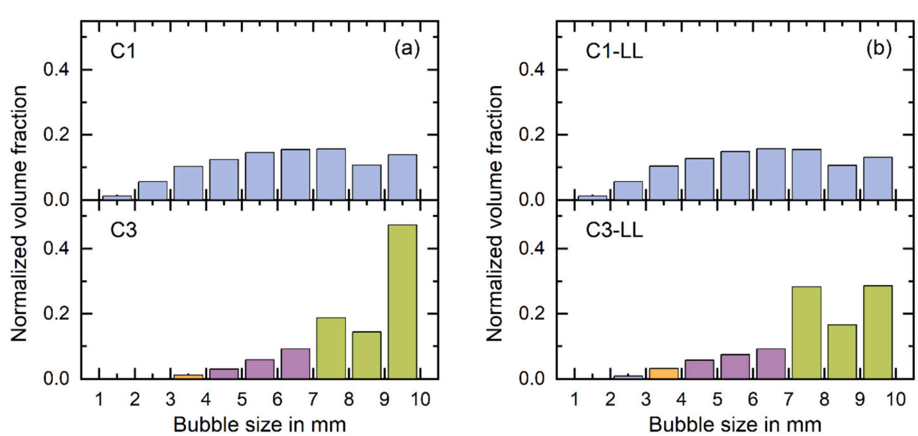

Fig. 10. Normalized bubble size distributions comparing the single-population (C1) and population-resolved multifluid (C3) class formulations at $u_{s,g,3} = 21.3$ mm s^{-1} and a height of 0.3 m. (a) Without lift (C1 top, C3 bottom). (b) With lift (C1-LL top, C3-LL bottom). Distributions are plane-averaged and time-averaged over 40–100 s.

(nine size classes and four transported moments); alternative class resolutions or higher-order moment representations would modify the absolute runtime but not the observed ranking between the investigated configurations. The corresponding numerical values are summarized in Table S6 in the Supplementary Information.

4. Discussion

The results of this study show how geometric confinement, interfacial-force modeling, and PBM formulation jointly determine the predictive performance of Euler-Euler-PBM simulations in pseudo-2D bubble columns. The shallow depth intensifies wall effects, enhances size-dependent bubble population segregation, and alters the balance of interfacial forces, making pseudo-2D systems a sensitive benchmark for evaluating CFD-PBM coupling strategies, particularly with respect to their ability to resolve size segregation.

4.1. Confinement Effects and Model Transferability

Pseudo-2D bubble columns impose hydrodynamic conditions that differ fundamentally from those in three-dimensional reactors used in real-life applications. Restricted depth suppresses transversal circulation, strengthens wall-driven gradients, and amplifies size-dependent population segregation. As a result, hydrodynamic behavior observed under shallow confinement cannot be directly transferred to three-dimensional configurations without explicit model reassessment.

In this context, the class method exhibits comparatively robust transferability. Since the class method resolves the bubble-size distribution explicitly rather than reconstructing bubble behavior from reduced statistical quantities, its predictions are less dependent on geometry-specific flow features than moment-based formulations, since the bubble-size distribution remains explicitly resolved. This explicit size resolution enables the class method to preserve size-dependent population-level trends more consistently when moving between confined pseudo-2D and fully three-dimensional systems.

By contrast, the Method-of-Moments approach is intrinsically coupled to the underlying flow field. Since the BSD is represented through a limited set of moments rather than discrete bubble populations with independent dynamics, Method-of-Moments predictions depend strongly on how accurately moment transport captures geometry-dependent segregation. As demonstrated in this study, confinement-induced gradients directly influence these structural assumptions, meaning that Method-of-Moments performance in three-dimensional reactors may differ substantially from its behavior in shallow geometries.

The present results demonstrate that transferability is not an inherent property of a PBM formulation. Rather it emerges from its interaction with geometry-specific hydrodynamics, with fundamentally different implications for class-based and moment-based approaches.

4.2. Interfacial Force Modeling under Confinement

Geometric confinement fundamentally alters the local balance of interfacial forces by steepening near-wall pressure gradients, suppressing transversal recirculation, and constraining bubble populations to pseudo-2D trajectories. Under such conditions, force correlations developed and calibrated for unconfined three-dimensional bubbly flows cannot be assumed to retain their predictive behavior. Thus, pseudo-2D configurations constitute a particularly stringent benchmark for the assessment of interfacial-force modeling in Euler-Euler simulations.

Among the modeled interfacial forces, the lateral lift force proved to be the most sensitive under confinement. While Tomiyama's lift correlation has been shown to perform well in fully three-dimensional bubbly flows (Tomiyama et al., 2002), its direct application to the present shallow geometry led to systematic deviations in the predicted population-dependent migration behavior. Experimental investigations of single bubbles rising in confined square and rectangular channels show that confinement significantly modifies bubble trajectories and wall-interaction dynamics, thereby altering the local interfacial force balance (Sirino et al., 2022). This suggests that the diameter-dependent lift characteristics embedded in classical formulations are not directly transferable to narrow or shallow columns.

Although confinement effects on bubble motion are well documented, no generally accepted lift formulation explicitly accounting for geometric confinement is currently available. Existing approaches are typically based on empirical corrections or case-specific calibration and lack systematic validation across different confined geometries. Introducing such modifications would therefore require additional assumptions and parameter tuning, increasing model uncertainty. For this reason, no confinement-specific correction of the lift force was applied in the present study.

In contrast, other interfacial forces considered here – drag, virtual mass, and turbulent dispersion – exhibited more stable behavior and did not display the same degree of sensitivity to confinement. Nevertheless, since these models were likewise developed for three-dimensional flow fields, their quantitative accuracy under shallow confinement cannot be assumed *a priori* and warrants careful evaluation.

Overall, the present results indicate that geometric confinement places disproportionate emphasis on the lateral lift force, which emerges as the dominant source of model uncertainty in pseudo-2D bubbly flows. Consequently, improving predictive fidelity in confined reactor systems will require lift formulations that explicitly account for confinement effects and modified near-wall dynamics, ideally supported by targeted experimental validation. Given the strong coupling between interfacial-force balance and population-resolved gas distribution, such developments are directly relevant to reliably predict mass transfer and hydrodynamics in confined gas-liquid reactors.

4.3. Representation of Size-Dependent Segregation in Multifluid Moment Methods

The population-resolved multifluid Method-of-Moments (MoM) formulation exhibited a markedly different behavior from the corresponding class-based multifluid approach. Despite employing separate dispersed populations and population-specific momentum balances, the predicted gas-holdup distributions, plume structures, and Sauter mean diameters of the individual populations remained comparatively similar, resulting in only limited size-dependent segregation.

As described in Section 2.5.2.2, the Direct Quadrature Method-of-Moments (DQMoM) implementation employed in this study couples the population balance model to a multifluid Euler-Euler framework through three dispersed gas populations. The transported moments are represented by quadrature-node diameters and weights that evolve through the DQMoM transport equations, while the hydrodynamic behavior of each dispersed population is governed by a population-specific momentum balance. In principle, this formulation enables size-dependent transport and hydrodynamic segregation and therefore provides a framework for representing bubble-population differentiation.

However, the present results indicate that the degree of differentiation achieved between the dispersed populations remains substantially weaker than in the corresponding class-based multifluid formulation. While the class-based approach produced clearly distinct gas-phase distributions and pronounced segregation between small and large bubbles, the multifluid MoM formulation yielded increasingly similar hydrodynamic behavior across the dispersed populations. As a consequence, the predicted segregation remained considerably weaker than that obtained with explicit size-class discretization.

This behavior can be attributed to the reduced representation of the bubble-size distribution inherent to moment methods. Since only a finite set of low-order moments is transported, the detailed shape of the distribution is not resolved explicitly. Consequently, different underlying size distributions may correspond to similar moment sets, reducing the ability of the model to maintain strongly separated bubble populations under conditions where hydrodynamic forces depend sensitively on bubble size.

The differences between the DQMoM and class-based formulations become particularly apparent in pseudo-2D bubble columns, where geometric confinement intensifies lateral segregation and steepens near-wall gradients. Under such conditions, small and large bubbles experience substantially different force balances: lift changes sign near characteristic diameters, turbulent dispersion depends on bubble size, and drag varies nonlinearly with diameter. The class-based multifluid formulation preserves these differences through discrete size classes and population-specific momentum balances. In contrast, the DQMoM formulation represents the size spectrum only through a limited set of transported moments, which reduces its ability to reproduce the pronounced size-dependent segregation predicted by the class-based approach.

The present results therefore suggest that the introduction of multiple hydrodynamic fields alone is not sufficient to guarantee accurate representation of size-dependent segregation. Under the investigated pseudo-2D conditions, explicit class-based discretization proved substantially more effective in preserving hydrodynamic differentiation between bubble populations than the corresponding DQMoM formulation.

Potential mitigation strategies include velocity-conditioned moment methods, multi-velocity quadrature formulations, and hybrid Euler-Lagrange approaches. While conceptually promising, these techniques involve substantially higher computational costs and are not yet widely available in commercial CFD solvers, which currently limits their applicability in engineering-scale bubble-column simulations.

4.4. PBM Selection and Implications for Reactor Design

The present comparison revealed clear differences in the suitability of PBM formulations for confined bubble-column flows. Class-based PBMs provided robust, population-resolved predictions under conditions characterized by pronounced hydrodynamic segregation, such as those encountered in pseudo-2D bubble columns. Consequently, they are particularly advantageous when accurate prediction of local gas distributions, interfacial area, plume structure, and size-dependent hydrodynamics is required. In contrast, Method-of-Moments-based PBMs remain attractive when computational efficiency is a priority and the degree of hydrodynamic size segregation is limited. Under such conditions, the reduced representation of the bubble-size distribution may provide an acceptable compromise between computational cost and predictive capability.

The results indicate that predictive capability is governed not only by the selected PBM formulation itself but also by the degree of hydrodynamic population resolution and its interaction with the surrounding modeling framework. While single-population approaches are capable of representing bubble-size evolution, the shared gas momentum equation limits their ability to reproduce size-dependent segregation mechanisms. Population-resolved multifluid formulations, in contrast, provide separate momentum balances for different bubble groups and therefore enable size-dependent hydrodynamic behavior to be represented explicitly.

However, the present results further demonstrate that the introduction of multiple dispersed populations alone does not necessarily guarantee accurate representation of size-dependent segregation. While the class-based multifluid formulation preserved pronounced hydrodynamic differentiation between bubble populations, the corresponding DQMoM formulation produced substantially weaker segregation despite employing population-specific momentum balances. This finding highlights that the mathematical representation of the bubble-size distribution is equally important as the hydrodynamic population resolution itself.

The sensitivity analyses further demonstrate that bubble-column predictions are not controlled by a single model component in isolation. Turbulence modeling, interfacial-force closures, breakup and coalescence kernels, hydrodynamic population resolution, and the admissible bubble-size range form a coupled modeling framework whose individual assumptions collectively determine the resulting bubble-size distribution and hydrodynamics. For example, extending the upper size boundary alters the predicted Sauter mean diameter, while having only a moderate influence on the overall gas holdup and leaving the observed differences between single-population and population-resolved formulations unchanged. This highlights that bubble-size metrics are generally more sensitive to modeling assumptions than bulk hydrodynamic quantities. Consequently, quantitative predictions may depend not only on the selected PBM formulation but also on the broader combination of turbulence, interfacial-force, and breakup-coalescence models employed.

Hydrodynamic population resolution should therefore be regarded as a key modeling parameter alongside the choice of turbulence closure, breakup and coalescence kernels, and interfacial-force models. Meaningful comparison of PBM approaches requires that these components are considered as part of a consistent overall modeling framework rather than as independent modeling choices.

From a reactor-design perspective, accurate prediction of the bubble-size distribution is essential because the BSD governs interfacial area, gas holdup, plume structure, and ultimately mass-transfer performance. The present results demonstrate that hydrodynamic population resolution can influence these quantities as strongly as the choice of breakup, coalescence, turbulence, or interfacial-force models. Consequently, the selection of a PBM formulation should not be viewed merely as a numerical implementation detail but as a central modeling decision affecting the predicted reactor behavior.

5. Conclusions

This work provides a systematic assessment of class-based and Method-of-Moments population balance formulations within single-population and population-resolved multifluid Euler-Euler simulations of a pseudo-2D bubble column. By exploiting a geometry that amplifies size-dependent hydrodynamics, the study isolates structural properties of PBM formulations that are difficult to diagnose in fully three-dimensional systems.

The results demonstrate that the mathematical representation of the bubble-size distribution has direct consequences for the predicted hydrodynamics. Although both the class-based and the Method-of-Moments approaches were implemented within population-resolved multifluid frameworks, their ability to reproduce size-dependent segregation differed substantially.

The class-based formulations preserved distinct bubble populations and reproduced the pronounced segregation behavior characteristic of confined bubbly flows. The single-population class method already provided accurate predictions of overall gas holdup and Sauter mean diameter, while the population-resolved multifluid extension additionally resolved size-dependent slip velocities and spatial segregation patterns. The central finding is therefore that class-based PBMs are structurally compatible with population-resolved hydrodynamics under confinement.

In contrast, the investigated Method-of-Moments formulations exhibited significant limitations under the present confined-flow conditions. The single-population formulation systematically overpredicted characteristic bubble sizes, while the multifluid DQMoM formulation produced increasingly similar gas populations despite their initially distinct size representations. As a result, the predicted plume structures, Sauter mean diameters, and gas-holdup distributions converged, leading to substantially weaker segregation than in the corresponding class-based formulation. This finding suggests that hydrodynamic population resolution alone is not sufficient to reproduce strongly segregating bubbly flows; the underlying representation of the bubble-size distribution remains equally important.

More generally, the results demonstrate that hydrodynamic population resolution constitutes a modeling parameter of comparable importance to the PBM formulation itself. Reliable prediction of segregating bubbly flows requires not only an adequate representation of bubble-size evolution but also an appropriate hydrodynamic treatment of bubble populations.

The results further demonstrate that pseudo-2D bubble columns are not simplified analogues of three-dimensional reactors but stringent benchmark systems that expose deficiencies in multiphase modeling approaches. Geometric confinement amplifies the coupling between interfacial forces, bubble-size representation, and momentum exchange, revealing structural incompatibilities that remain obscured in less segregated flow configurations.

Sensitivity analyses showed that turbulence modeling, interfacial-force closures, breakup and coalescence kernels, hydrodynamic population resolution, and the admissible bubble-size range form a coupled modeling framework. While the imposed upper size limit affected quantitative bubble-size metrics such as the Sauter mean diameter, the qualitative differences between single-population and population-resolved formulations remained unchanged. The central conclusions regarding hydrodynamic segregation and PBM performance were therefore robust with respect to the investigated modeling assumptions.

With respect to interfacial forces, the lateral lift force was found to introduce additional uncertainty under confinement and did not compensate for limitations of the underlying PBM formulation. In several cases, lift degraded predictive accuracy, underscoring that classical lift correlations developed for unconfined three-dimensional flows cannot be assumed transferable to shallow geometries.

From an engineering perspective, these findings imply that PBM selection must be guided explicitly by reactor geometry and the degree of hydrodynamic segregation. Class-based PBMs are required whenever size-dependent transport, segregation, or interfacial area distribution are critical to reactor performance, as in confined or strongly heterogeneous systems. Method-of-Moments approaches remain useful for large-scale simulations focused on global trends, but only in regimes where size-conditioned hydrodynamics play a subordinate role.The present work provides new insight into the interplay between PBM structure, hydrodynamic population resolution, and confinement-induced segregation in bubbly flows. By systematically separating the effects of bubble-size representation and hydrodynamic population resolution within a consistent CFD-PBM framework, the study identifies structural limitations of current DQMoM-based multifluid implementations and demonstrates that hydrodynamic population resolution can influence predictive capability as strongly as the selected PBM formulation itself.

These findings are directly relevant for predictive modeling of multiphase reactors in emerging low-carbon process routes, including CO_2 capture and utilization, hydrogen-based synthesis, Power-to-X processes, and intensified gas-liquid reactor concepts. Future work should extend the validation to different levels of geometric confinement and focus on population-balance formulations and interfacial-force closures specifically designed for confinement-dominated bubbly flows.

CRediT authorship contribution statement

Lydia Becka: Writing – original draft, Visualization, Validation, Software, Methodology, Investigation, Formal analysis, Data curation. **Yannik Danner:** Writing – review & editing, Visualization, Software, Methodology, Data curation. **Ralf Peters:** Writing – review & editing, Supervision, Resources, Project administration, Funding acquisition, Conceptualization. **Thomas E. Müller:** Writing – review & editing, Visualization, Validation, Supervision, Formal analysis, Conceptualization.

Declaration of competing interest

The authors declare that they have no known competing financial interests or personal relationships that could have appeared to influence the work reported in this paper.

Acknowledgements

The authors are grateful to their colleagues in the fuel synthesis departments at Jülich, as well as to all project and cooperation partners for the stimulating scientific exchange.

T.E.M. acknowledges funding from the State of North Rhine-Westphalia, grant number IRR-2018-1, RWE Power AG and the Faculty of Mechanical Engineering of Ruhr-Universität Bochum, as part of the endowed chair Carbon Sources and Conversion (CSC).

The financial support of the Bundesministerium für Wirtschaft und Klimaschutz (BMWK, now Bundesministerium für Wirtschaft und Energie, BMWE) for the project ECO_2Feed (grant number 03EE5126B) is gratefully acknowledged.

We acknowledge support from the DFG Open Access Publication Funds of the Ruhr-Universität Bochum.

Appendix A. Supplementary data

Supplementary data to this article can be found online at https://doi.org/10.1016/j.ces.2026.124805.

Data availability

Data will be made available on request.

References

Alopaeus, V., Koskinen, J., Keskinen, K.I., Majander, J., 2002. Simulation of the population balances for liquid–liquid systems in a nonideal stirred tank. Part 2—parameter fitting and the use of the multiblock model for dense dispersions. Chem. Eng. Sci. 57, 1815–1825.

Anderson, J.D., 2002. *Computational Fluid Dynamics: The Basics with Applications*. McGraw-Hill, New York.

ANSYS Inc., *ANSYS Fluent User's Guide*, Release 2022 R1, Canonsburg, PA (2022).

Artz, J., Müller, T.E., Thenert, K., Kleinekorte, J., Meys, R., Sternberg, A., Bardow, A., Leitner, W., 2018. Sustainable conversion of carbon dioxide: an integrated review of catalysis and life cycle assessment. Chem. Rev. 118, 434–504.

Becker, S., De Bie, H., Sweeney, J., 1999. Dynamic flow behaviour in bubble columns. Chem. Eng. Sci. 54, 4929–4935.

Besagni, G., Inzoli, F., Ziegenhein, T., 2018. Two-phase bubble columns: a comprehensive review. ChemEngineering 2, 13.

Borchers, O., Eigenberger, G., 2004. Detailed experimental studies on gas–liquid bubble flow in bubble columns with and without recycle. In: *Bubbly Flows: Analysis, Modelling and Calculation*. Springer, Berlin, pp. 1–10.

Buffo, A., Vanni, M., Marchisio, D.L., Fox, R.O., 2013. Multivariate quadrature-based moments methods for turbulent polydisperse gas–liquid systems. Int. J. Multiphase Flow 50, 41–57.

Buffo, A., De Bona, J., Vanni, M., Marchisio, D.L., 2016. Simplified volume-averaged models for liquid–liquid dispersions: correct derivation and comparison with other approaches. Chem. Eng. Sci. 153, 382–393.

A. D. Burns, T. Frank, I. Hamill, J.-M. Shi, "The Favre-averaged drag model for turbulent dispersion in Eulerian multi-phase flows," in: *Proc. 5th Int. Conf. Multiphase Flow (ICMF)*, Yokohama, Japan (2004).

Buwa, V.V., Ranade, V.V., 2002. Dynamics of gas–liquid flow in a rectangular bubble column: experiments and single/multi-group CFD simulations. Chem. Eng. Sci. 57, 4715–4736.

Cachaza, E.M., Díaz, M.E., Montes, F.J., Galán, M.A., 2008. Analytical solution of the mass conservation equations in gas–liquid systems: applicability to the evaluation of the volumetric mass transfer coefficient (kLa). Ind. Eng. Chem. Res. 47, 4510–4522.

Cachaza, E.M., Díaz, M.E., Montes, F.J., Galán, M.A., 2009. Simultaneous computational fluid dynamics simulation of the hydrodynamics and mass transfer in a partially aerated bubble column. Ind. Eng. Chem. Res. 48, 8685–8696.

Cheng, Y., Zhang, Q., Jiang, P., Zhang, K., Wei, W., 2020. Investigation of plume offset characteristics in bubble columns by Euler–Euler simulation. Processes 8, 795.

Clift, R., Grace, J.R., Weber, M.E., 2005. *Bubbles, Drops, and Particles*. Dover Publications, Mineola, NY.

Coulaloglou, C.A., Tavlarides, L.L., 1977. Description of interaction processes in agitated liquid–liquid dispersions. Chem. Eng. Sci. 32, 1289–1297.
Date, A.W., 2005. *Introduction to Computational Fluid Dynamics*. Cambridge University Press, Cambridge.
Díaz, M.E., Montes, F.J., Galán, M.A., 2008. Experimental study of the transition between unsteady flow regimes in a partially aerated two-dimensional bubble column. Chem. Eng. Process. 47, 1867–1876.
Fletcher, D.F., McClure, D.D., Kavanagh, J.M., Barton, G.W., 2017. CFD simulation of industrial bubble columns: numerical challenges and model validation successes. Appl. Math. Model. 44, 25–42.
Geary, N.W., Rice, R.G., 1991. Bubble size prediction for rigid and flexible spargers. AIChE J. 37, 161–168.
Hessenkemper, H., Ziegenhein, T., Rzehak, R., Lucas, D., Tomiyama, A., 2021. Lift force coefficient of ellipsoidal single bubbles in water. Int. J. Multiphase Flow 138, 103587.
Hlawitschka, M., 2013. *Computational Fluid Dynamics Aided Design of Stirred Liquid–Liquid Extraction Columns*. Technische Universität Kaiserslautern, Kaiserslautern, Germany. PhD thesis.
Hlawitschka, M.W., Schäfer, J., Hummel, M., Garth, C., Bart, H.-J., 2016. Population balance modelling using a multiphase-CFD code and comparing visualization. Chem. Ing. Tech. 88, 1480–1491.
Joshi, J.B., 2001. Computational flow modelling and design of bubble column reactors. Chem. Eng. Sci. 56, 5893–5933.
Khan, K.I., 2014. *Fluid Dynamic Modelling of Bubble Column Reactors*. Politecnico di Torino, Turin, Italy. PhD thesis.
Krepper, E., Lucas, D., Frank, T., Prasser, H.-M., Zwart, P.J., 2008. The inhomogeneous MUSIG model for the simulation of polydispersed flows. Nucl. Eng. Des. 238, 1690–1702.
Kumar, S., Ramkrishna, D., 1996. On the solution of population balance equations by discretization—I. A fixed pivot technique. Chem. Eng. Sci. 51, 1311–1332.
L. Gemello, *Modelling of the Hydrodynamics of Bubble Columns Using a Two-Fluid Model Coupled with a Population Balance Approach*, PhD thesis, Université Claude Bernard Lyon 1, Lyon, France and Politecnico di Torino, Turin, Italy (2018).
Laakkonen, M., Alopaeus, V., Aittamaa, J., 2006. Validation of bubble breakage, coalescence and mass transfer models for gas–liquid dispersion in agitated vessel. Chem. Eng. Sci. 61, 218–228.
Lehr, F., Millies, M., Mewes, D., 2002. Bubble-size distributions and flow fields in bubble columns. AIChE J. 48, 2426–2443.
Liao, Y., Lucas, D., 2009. A literature review of theoretical models for drop and bubble breakup in turbulent dispersions. Chem. Eng. Sci. 64, 3389–3406.
Liao, Y., Lucas, D., 2010. A literature review on mechanisms and models for the coalescence process of fluid particles. Chem. Eng. Sci. 65, 2851–2864.
Lide, D.R., 2009. *CRC Handbook of Chemistry and Physics*. CRC Press, Boca Raton, FL.
Liu, Y., Hinrichsen, O., 2014. Study on CFD–PBM turbulence closures based on k–ε and Reynolds stress models for heterogeneous bubble column flows. Comput. Fluids 105, 91–100.
Liu, L., Yan, H., Ziegenhein, T., Hessenkemper, H., Li, Q., Lucas, D., 2019. A systematic experimental study and dimensionless analysis of bubble plume oscillations in rectangular bubble columns. Chem. Eng. J. 372, 352–362.
Lucas, D., Frank, T., Lifante, C., Zwart, P., Burns, A., 2011. Extension of the inhomogeneous MUSIG model for bubble condensation. Nucl. Eng. Des. 241, 4359–4367.
Lucas, D., Krepper, E., Liao, Y., Rzehak, R., Ziegenhein, T., 2020. General guideline for closure model development for gas-liquid flows in the multi-fluid framework. Nucl. Eng. Des. 357, 110396.
Lucas, D., Ziegenhein, T., 2019. Influence of the bubble size distribution on the bubble column flow regime. Int. J. Multiphase Flow 120, 103092.
Luo, H., Svendsen, H.F., 1996. Theoretical model for drop and bubble breakup in turbulent dispersions. AIChE J. 42, 1225–1233.
Luo, H., Coalescence, 1995. *Breakup and Liquid Circulation in Bubble Column Reactors*. Norwegian Institute of Technology (NTH), Trondheim, Norway. PhD thesis.
Mappas, V.K., Dorneanu, B., Heinzelmann, N., Schnitzlein, K., Arellano-García, H., 2025. An efficient and unified modeling framework for trickle bed reactors: a modular approach. Chem. Eng. Technol. 39, 1110–1126.
Marchisio, D.L., Fox, R.O., 2007. *Multiphase Reacting Flows: Modelling and Simulation*. Springer, Berlin.
Marchisio, D.L., Fox, R.O., 2013. *Computational Models for Polydisperse Particulate and Multiphase Systems*. Cambridge University Press, Cambridge.
Markewitz, P., Kuckshinrichs, W., Leitner, W., Linssen, J., Zapp, P., Bongartz, R., Schreiber, A., Müller, T.E., 2012. Worldwide innovations in the development of carbon capture technologies and the utilization of CO2. Energy Environ. Sci. 5, 7281–7305.
Martínez-Bazán, C., Montañés, J.L., Lasheras, J.C., 1999. On the breakup of an air bubble injected into a fully developed turbulent flow. Part 1. Breakup frequency. J. Fluid Mech. 401, 157–182.
McClure, D.D., Kavanagh, J.M., Fletcher, D.F., Barton, G.W., 2013. Development of a CFD model of bubble column bioreactors: part one—a detailed experimental study. Chem. Eng. Technol. 36, 2065–2070.
McClure, D.D., Kavanagh, J.M., Fletcher, D.F., Barton, G.W., 2014. Development of a CFD model of bubble column bioreactors: part two—comparison of experimental data and CFD predictions. Chem. Eng. Technol. 37, 131–140.
Michaelides, E.E., Sommerfeld, M., Van Wachem, B., 2022. *Multiphase Flows with Droplets and Particles*. CRC Press, Boca Raton, FL.
Narsimhan, G., Gupta, J.P., Ramkrishna, D., 1979. A model for transitional breakage probability of droplets in agitated lean liquid–liquid dispersions. Chem. Eng. Sci. 34, 257–265.
Pacek, A.W., Man, C.C., Nienow, A.W., 1998. On the Sauter mean diameter and size distributions in turbulent liquid/liquid dispersions in a stirred vessel. Chem. Eng. Sci. 53, 2005–2011.
Petitti, M., Nasuti, A., Marchisio, D.L., Vanni, M., Baldi, G., Mancini, N., Podenzani, F., 2010. Bubble size distribution modeling in stirred gas–liquid reactors with QMOM augmented by a new correction algorithm. AIChE J. 56, 36–53.
Pfleger, D., Becker, S., 2001. Modelling and simulation of the dynamic flow behaviour in a bubble column. Chem. Eng. Sci. 56, 1737–1747.
Prince, M.J., Blanch, H.W., 1990. Bubble coalescence and break-up in air-sparged bubble columns. AIChE J. 36, 1485–1499.
Ramkrishna, D., 2000. *Population Balances: Theory and Applications to Particulate Systems in Engineering*. Elsevier, Amsterdam.
Robinius, M., Otto, A., Heuser, P., Welder, L., Syranidis, K., Ryberg, D.S., Grube, T., Markewitz, P., Peters, R., Stolten, D., 2017. Linking the power and transport sectors—Part 1: The principle of sector coupling. Energies 10, 956.
Roghair, I., Van Sint Annaland, M., Kuipers, H.J.A.M., 2013. Drag force and clustering in bubble swarms. AIChE J. 59, 1791–1800.
Rzehak, R., Krepper, E., Liao, Y., Ziegenhein, T., Kriebitzsch, S., Lucas, D., 2015. Baseline model for the simulation of bubbly flows. Chem. Eng. Technol. 38, 1972–1978.
Rzehak, R., Krauß, M., Kováts, P., Zähringer, K., 2017. Fluid dynamics in a bubble column: new experiments and simulations. Int. J. Multiphase Flow 89, 299–312.
Sanyal, J., Marchisio, D.L., Fox, R.O., Dhanasekharan, K., 2005. On the comparison between population balance models for CFD simulation of bubble columns. Ind. Eng. Chem. Res. 44, 5063–5072.
Shah, Y.T., Kelkar, B.G., Godbole, S.P., Deckwer, W.-D., 1982. Design parameters estimations for bubble column reactors. AIChE J. 28, 353–379.
Sirino, T., Machado, V., Mancilla, E., Morales, R.E.M., 2022. Dynamics of single bubbles rising in confined square and rectangular channels. Int. J. Multiphase Flow 157, 104257.
Tomiyama, A., 1998. Struggle with computational bubble dynamics. Multiph. Sci. Technol. 10, 369–405.
Tomiyama, A., Tamai, H., Zun, I., Hosokawa, S., 2002. Transverse migration of single bubbles in simple shear flows. Chem. Eng. Sci. 57, 1849–1858.
Tomkins, P., Müller, T.E., 2019. Evaluating the carbon inventory, carbon fluxes and carbon cycles for a long-term sustainable world. Green Chem. 21, 3994–4013.
Upadhyay, R.K., Pant, H.J., Roy, S., 2013. Liquid flow patterns in rectangular air–water bubble column investigated with radioactive particle tracking. Chem. Eng. Sci. 96, 152–164.
Wang, T., Wang, J., 2017. Multiphase flow reactors for methanol and dimethyl ether production. In: *Multiphase Reactor Engineering for Clean and Low-Carbon Energy Applications*. Elsevier, Amsterdam, pp. 189–218.
Weiske, S., 2022. *Evaluation von Reaktorkonzepten für die CO2-basierte Methanolsynthese aus Wasserstoff und Kohlendioxid mithilfe von CFD-Simulationen*. RWTH Aachen University, Aachen, Germany. PhD thesis.
Wilkinson, P.M., Spek, A.P., van Dierendonck, L.L., 1992. Design parameters estimation for scale-up of high-pressure bubble columns. AIChE J. 38, 544–554.
Xu, L., Yuan, B., Ni, H., Chen, C., 2013. Numerical simulation of bubble column flows in churn-turbulent regime: comparison of bubble size models. Ind. Eng. Chem. Res. 52, 6794–6802.
Yakhot, V., Orszag, S.A., 1986. Renormalization group analysis of turbulence. J. Sci. Comput. 1, 3–51.
Zhang, X.-B., Yan, W.-C., Luo, Z.-H., 2020. CFD–PBM simulation of bubble columns: sensitivity analysis of the non-drag forces. Ind. Eng. Chem. Res. 59, 18674–18682.
Zhang, L., Zhou, Z., Shao, X., 2020. Numerical investigation on the drag force of a single bubble and bubble swarm. J. Hydrodyn. 32, 1043–1049.
Ziegenhein, T., Lucas, D., 2019. The critical bubble diameter of the lift force in technical and environmental, buoyancy-driven bubbly flows. Int. J. Multiphase Flow 116, 26–38.
Ziegenhein, T., Tomiyama, A., Lucas, D., 2018. A new measuring concept to determine the lift force for distorted bubbles in low Morton number system: results for air/water. Int. J. Multiphase Flow 108, 11–24.